Differential scanning calorimetry and NMR study of water confined in a mesoporous bioactive glass

Abdelkarim Rjiba, Hassan Khoder, Jawhar Jelassi, Sabine Bouguet-Bonnet, Carole Gardiennet, El-Eulmi Bendeif, Axel Gansmüller, Rachida Dorbez-Sridi

Differential scanning calorimetry and NMR study of water confined in a mesoporous bioactive glass

Abdelkarim Rjiba[1], Hassan Khoder[2], Jawhar Jelassi[1], Sabine Bouguet-Bonnet[2], Carole Gardiennet[2], El-Eulmi Bendeif [2*], Axel Gansmüller [2*] and Rachida Dorbez-Sridi [1]

[1]Université de Monastir, Laboratoire Physico-Chimie des Matériaux, 5019 Monastir, Tunisie.

[2]Université de Lorraine, CNRS CRM2, F-54000 Nancy, France

**Correspondence e-mail: axel.gansmuller@univ-lorraine.fr, el-eulmi.bendeif@univ-lorraine.fr*

ABSTRACT:

The emergence of a new generation of nanostructured materials opened a wide range of new potential applications for Bioglasses such as DNA vaccination, cellular treatment or drug delivery with a well-controlled loading and release of (bio)active molecules. In this study we compare structural, dynamic and thermal properties of water confined in two $CaO-SiO_2-P_2O_5$ mesoporous bioactive glasses (MBGs). One of the MBGs is prepared by standard sol-gel methods and the other by microfluidic procedures, therefore both MBGs have the same molar compositions (92% SiO_2, 6% CaO, and 2% P_2O_5) but different textural properties (surface areas, porous volume and grain architecture). These materials are intended to interact with body fluids which are essentially composed of water, it is therefore crucial to understand the water-MBG interaction. With this objective, we apply a complementary

approach based on ^{1}H field-cycling NMR relaxometry, ^{1}H magic-angle spinning NMR spectroscopy and differential scanning calorimetry (DSC). With low-field relaxometry we observe that adsorbed water has the same behavior in the mesoporous channels of both systems, but that the escaping of water molecules towards the bulk is slightly faster in the microfluidic material. By combining ^{1}H MAS NMR and DSC to study a series of MBG samples at variable temperature and water content, we observe that for low temperature and low water content, pooling of water molecules is less pronounced in the case of the microfluidic MBG. All our results therefore point towards a microcapsule organization of the microfluidic MBG that provides better water access to the full porous volume.

KEYWORDS: ^{1}H MAS NMR, ^{1}H field-cycling NMR relaxometry, DSC, mesoporous bioactive glasses, nanoconfined water

1. INTRODUCTION:

Since their discovery, bioactive glasses (BGs) have been used as bone-tissue regeneration systems[1]. In the last decade, the emergence of a new generation of nanostructured materials named mesoporous bioactive glasses (MBGs) opened a wide range of new potential applications for BGs such as drug and gene deliveries[2], DNA vaccination or cellular treatment. When exposed to body fluids $CaO{-}SiO_2{-}P_2O_5$ MBGs develop a bone-bonding surface layer that initially consists of amorphous calcium phosphate (ACP), which transforms into hydroxy-carbonate apatite (HCA) with a very similar composition to bone/teeth mineral[3]. These materials are characterized by a high bioactivity response (i.e. faster formation of HCA layers) due to the incorporation of Ca and P atoms in the SiO_2 network[4,5]. These materials are intended to interact with body fluids which are essentially composed of water. Hence, it is of great importance to study and understand the dynamic of confined water in the MBGs.

In the vicinity of the mesoporous materials confining surface, the structural and dynamical properties of confined water change as compared to bulk water. Since confinement in narrow pores also affects the structural and dynamical properties of water, it has also consequences on the phase transitions. In particular there is a strong decrease in the freezing temperature of water in confinement, the melting temperature being lowered by more than 50 K depending on the pore size[6–8].

The present work concerns two types of $CaO{-}SiO_2{-}P_2O_5$ mesoporous glasses based on conventional silica mesoporous materials such as SBA-15. The first MBG type, classed as “standard MBG”, is synthesized by standard sol-gel techniques and exhibits a two

dimensional hexagonal mesoporous structure[9]. The second MBG system, classed as "microfluidic MBG", is synthesized by droplet based microfluidics and ESE techniques (Combined Emulsion and Solvent Evaporation)[10]; it displays microcapsules with a 2D-hexagonal mesoporous organized shell[11]. Our aim is to investigate the effect of grain architecture (with or without cavities) on the dynamics and the structural organization of water confined in the pores of these two MBGs that have the same composition but are made with different methods. Several experimental techniques such as Raman spectroscopy[12], Quasi-elastic neutron scattering (QENS)[13], Inelastic Neutron Scattering (INS) and Deep Inelastic Neutron Scattering (DINS)[14] have been employed to study the dynamical behavior of water confined in micro and mesoporous materials. These studies evidenced the slowing down of the translational and rotational motion upon confinement and showed that water molecules in the pores are less mobile than those in bulk. Moreover, it has been shown that the mobility of confined water molecules is decreased by narrowing of the pore size.

Here we investigate structural, dynamical and thermal properties of confined water inside two MBGs by applying a powerful approach combining Differential Scanning Calorimetry, field-cycling NMR relaxometry and ^{1}H magic-angle spinning NMR spectroscopy[15].

NMR relaxometry is well-known as a noninvasive technique consisting in measuring the ^{1}H longitudinal relaxation rate R_1 as a function of the measurement frequency, or equivalently of the static B_0 magnetic field. It provides a powerful approach for identifying the different regimes of water dynamics and it has been widely used for studying in situ water behavior in porous media[16,17]. NMRD profiles (R_1 versus ν_H, where ν_H is the proton

Larmor frequency) are obtained at low field (ν_H < 10 MHz) by use of the fast field-cycling technique[18]. In the case of sufficiently slow motion, as for confined water, longitudinal relaxation rates are frequency-dependent and a dispersion can be observed in the NMRD profile when the quantity $2\pi\nu_H\tau_c$ is in the same order than unity (where τ_c is an effective correlation time describing the motion). On the contrary, in the case of bulk water no dispersion is observed in ^{1}H longitudinal relaxation rate because of the fast rotational diffusion of water molecules (the so-called extreme narrowing condition: $2\pi\nu_H\tau_c << 1$). In the present work, NMR relaxometry was used for comparing the water dynamical behavior inside two MBGs, the standard and the microfluidic one.

In addition to ^{1}H NMR relaxation, it is well known that the interaction of a water molecule with its surroundings is reflected in ^{1}H NMR chemical shifts which therefore provide a picture of the intermolecular geometry and in particular the local hydrogen bond geometry[19]. Nevertheless, this information is only available if the different ^{1}H sites are sufficiently resolved on the NMR spectra. Whereas in liquid samples the fast isotropic motion of the molecules completely averages out the anisotropic interactions, responsible for the typically broad ^{1}H signals, these interactions are partly averaged out in the solid state by spinning the sample at the so called “magic angle” in MAS NMR[20]. Because of the strong homonuclear ^{1}H dipolar couplings, this is usually not sufficient to obtain narrow ^{1}H lines and resolve the spectra completely. In the present study, we bypass this problem by working with the residual ^{1}H signal from deuterated water HOD, (~0.1 %) and therefore prevent homonuclear dipolar couplings that occur between close ^{1}H spins. Information from chemical shift anisotropy (CSA) (e.g. rotational dynamics) nevertheless remains accessible through

the spinning sideband pattern, without degrading the spectral resolution. Additionally, the peak positions and linewidths in the ^{1}H NMR spectra of interfacial water is also influenced by the mobility of the molecules and their interaction with surface groups or charged sites, depending on the structure of the hydrogen bond network and the distance between molecules and surface sites[21]. To prevent the line broadening resulting from conformational changes happening on the timescale of the NMR measurements (typically ms timescale), we also perform measurements at temperatures below the phase transitions observed on DSC thermograms, in order to identify and compare how the water structures inside our two types of MBGs. As a consequence, we can make use of Solid-state ^{1}H NMR as a powerful technique to study the different water environments inside the mesopores of silica which are characterized by their individual chemical shift. In particular, the originality of this work lies in taking advantage of residual ^{1}H nuclei present in deuterated water to avoid strong homonuclear dipolar couplings at low temperature.

^{1}H magic-angle spinning NMR spectroscopy (MAS-NMR) has been applied several times to characterize different hydration sites at the vicinity of pore surfaces[22], to study various interactions between water molecules and surface hydroxyl groups[21], and to study pore-filling mechanisms[23]. Phase transition of confined water was also extensively studied experimentally by differential scanning calorimetry (DSC) which is one of the most convenient and effective methods to study phase changes in materials. In particular, it has been employed in the study of water confined in mesoporous materials, such as silica gel, MCM-41, SBA-15[6,24,25], as well as in combination with ^{2}H NMR[26–28] . Differential scanning calorimetry measurements of water freezing in incompletely filled silica pores has shown evidence for a fragile to strong transition related to adsorbed water layers[29] and experimental

dynamic results were combined with DSC measurement by Zanotti et al to show the existence of a liquid-liquid transition or reorganization involving adsorbed water[30].

In this study we observe a similar behavior of water inside the MBGs that exhibits two different dynamical regimes in the pore center and at the pore surface. In particular the combination of DSC, ^{1}H relaxometry and MAS NMR, allows to highlight the effect of grain architecture on the dynamics and the structuring of confined water molecules, as well as on the phase transitions taking place between 300 K and 200 K.

2. EXPERIMENTAL METHODS:

2.1. Synthesis of the MBGs

The two MBGs have the same molar composition (92 % SiO_2, 6 % CaO, and 2 % P_2O_5), the standard MBG was synthesized using the standard sol-gel technique , it was elaborated using P123 by a two-step acid-catalyzed self-assembly process combined with hydrothermal treatment in an inorganic–organic system[9]. The microfluidic MBG was synthesized using a new microfluidic-assisted method based on the combination of the solvent evaporation method and the use of highly monodisperse droplets as soft-templates. This microfluidic approach allows the fabrication of well-defined highly monodisperse and MBG microspheres with a controllable size in the micrometer range[11]. Tetraethyl orthosilicate (TEOS) (99 %; Sigma-Aldrich, France) was used as a silica source, Pluronic P123 amphiphilic block copolymer (PEG-PPG-PEG, Molar mass: 5800 g/mol, Sigma-Aldrich, France) was used as a mesostructuring template. The silica sol precursor was prepared by dissolving, under stirring, 1 g of P123 in 20 ml of 2 M HNO_3 solution and 5 ml of distilled water, until the solution became clear. Then 3.6 g of TEOS, 0.16 g of TEP and 0.53 g of $CaCO_3$ were added to the solution respectively one by one after vigorous stirring. After 3 hours stirring was stopped and the synthesis was completed by the microfluidic method[11]. After synthesis, all materials were stored together inside a desiccator to prevent hydrolysis at the pore surface.

2.2 Morphological characterization of MBGs:

The hexagonal channel array of the two MBGs was confirmed by small angle X-ray scattering (SAXS) and the textural properties were determined by nitrogen adsorption-desorption and BET measurements (table 1) [11]

Sample	S_{BET}(m^2/g)	V_P (cm^3/g)	D_P(nm)
Microfluidic MBG	**514**	**0.76**	**5.9**
Standard sol-gel MBG	**376**	**0.66**	**5.7**

Table 1. Textural parameters of MBGs: Specific surface area (S_{BET}), mesopore volume (V_P) and pore size (D_P), synthesized by combining sol gel and Microfluidic Method (Microfluidic MBG) and by standard sol-gel method (Standard MBG)

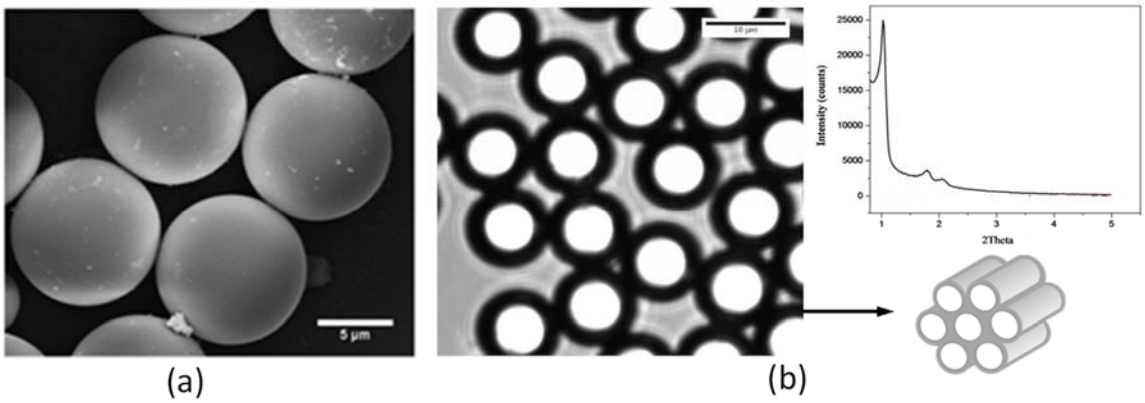

Figure1. a) SEM micrograph of the microfluidic MBG b) White field confocal microscopy images of the microfluidic MBG sample doped with fluorescein

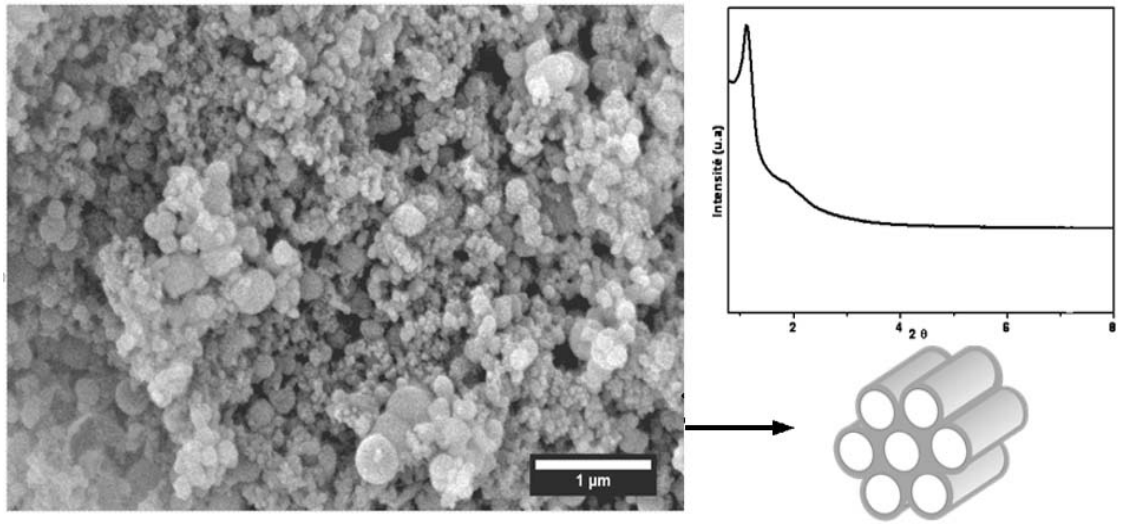

Figure2. SEM micrograph of the standard sol-gel MBG surface

The microfluidic MBG microcapsules exhibit a soft-like thin shell with a thickness of about 1 µm, across which 5.9 nm sized mesopores form a well-ordered hexagonal 2D network (figure 1)[11], the opening of mesopores at both ends across the microcapsules shell is confirmed. In contrast particles of the standard sol-gel MBG have a dense appearance, and high degree of coalescence (Figure 2)[9]. The average particle size is about 0.1 µm. The distance between two interconnected cylindrical pores is estimated as the inverse length of scattering vector in X-ray diffraction is about 9.2 nm in the case of the standard MBG and about 9.8 nm in the case of the microfluidic MBG.

2.3 Sample Preparation and Measurements:

2.3.1 NMR relaxometry measurement:

Bioglass powders (microfluidic and sol-gel MBG) were dried during one day at 150 °C before hydration with the wanted volume of distilled water : volumic filling degrees f of 33

% vol, 66 % vol and 99 % vol were used (f corresponds to the ratio of added water and the mesoporous volume of the sample). Samples were then kept at 25°C during 1 night for complete equilibrium before ^{1}H relaxometry measurement. They were prepared in 8 mm o.d. hermetically sealed capsules in order to avoid any water loss during the measurements. An additional sample was made with the microfluidic bioglass filled at f = 99 % with heavy water D_2O (99.9 atom % D).

^{1}H NMRD profiles (i.e. longitudinal relaxation rate R_1 as a function of the proton Larmor frequency), were acquired between 5 kHz and 10 MHz on a Stelar Smartracer fast-field-cycling relaxometer (Stelar company, Medde, Italy). Temperature was fixed at 25 °C. For all R_1 measurements, magnetization recovery curves were found to be monoexponential within the experimental errors. 32 different values of the static magnetic field were sampled, with a fixed acquisition field of 7.2 MHz (^{1}H Larmor frequency). Pre-polarized measurements were done between 5 kHz and 4 MHz with a polarization duration of 0.7 s at a ^{1}H frequency of 8 MHz, and non-polarized sequence was used between 4 MHz and 10 MHz. Field-switching time was 3 ms. For each B_0 value, R_1 were obtained from the magnetization monoexponential evolution as a function of the time, sampled with 16 values between 0.01 and 4 times the longitudinal relaxation time. 64 accumulations were used for all measurements (excepted for the measurement of residual proton dispersion in the microfluidic bioglass filled with D_2O, where 192 accumulations were done), and a recycle delay of 1 s was applied.

2.3.2 ^{1}H magic-angle spinning NMR measurement:

The sample preparation was similar to the procedure used for relaxometry measurements. Several bioglass powders (standard and microfluidic) were packed simultaneously in open separate MAS NMR rotors and dried together during one day at 150 °C at a pressure of 10^{-4} mbar. The dried samples were then rehydrated with the wanted volume of heavy water D_2O (99.9 atom % D). The exact volumic filling factor f was determined by comparing the weight of the dry powders with the weight upon hydration using a Mettler Toledo Excellence XS105 analytical balance with a precision of 0.01 mg. The NMR rotors were then kept closed at 25 °C during 1 day for complete equilibrium before ^{1}H MAS measurements. NMR analysis was performed on a high-field Bruker NMR AVANCE III spectrometer operating at 14 T (^{1}H NMR frequency, 600 MHz) with a Bruker 2.5 mm MAS double resonance probe. The rf field strength applied for the ^{1}H pulse was set to 86.2 kHz with an excitation pulse duration of 2.9 µs. The interscan delay was set to 3 s and 16-64 scans were accumulated depending on the experiments. ^{1}H chemical shifts were referenced relative to TMS. Room temperature experiments were performed at a MAS frequency of 12.5 kHz whereas for low temperature experiments the MAS was kept at 9 kHz. Cooling of the MAS sample was performed using N_2 gas pre-cooled inside a home-made temperature exchange Dewar. Sample temperature was monitored by the stator output thermocouple in the Bruker thermal control system. The real sample temperature was calibrated externally by measuring the variation in ^{79}Br chemical shift for a KBr sample plotted against the Bruker temperature display [31]. Variable-temperature experiments were performed by decreasing the sample temperature and waiting at least 30 min for the temperature to equilibrate before each measurement was performed. The temperature settings were precise to ±0.1 °C. For the quantitative measurements, the probe and rotor ^{1}H

background was subtracted from the spectra after measuring the ^{1}H signature of the empty rotors. The DMFIT program [32] was used for spectral deconvolution and for fitting ^{1}H chemical shift anisotropy.

2.3.3 DSC measurement:

The differential scanning calorimetry (DSC) experiments were performed on DSC1 Mettler-Toledo instrument equipped with a high sensitivity DSC HSS8 sensor. The instrument had been previously calibrated at a scanning rate of 5 K. min^{-1} with water and indium. Samples at 13 % vol, 29 % vol, 79 % vol and 105 % vol of microfluidic MBG and at 15 % vol, 38 % vol, 91 % vol and 121 % vol of sol-gel MBG were prepared by weighting appropriate amounts of dried MBGs and contacted with an appropriate quantity of water corresponding to the desired volume hydration level. The aluminum pans were then sealed, reweighed, and submitted to two subsequent cooling-heating cycles in the 293-213 K temperature range. The measurements were made under nitrogen at atmospheric pressure and the cooling and heating scan rates were kept at 5 $K.min^{-1}$. Well-separated DSC peaks for the freezing/melting of confined water in the pores were obtained.

3. RESULTS AND DISCUSSION :

3.1 ^{1}H NMRD profiles:

The ^{1}H experimental dispersion curves for the three filling degrees (99 % vol, 66 % vol, and 33 % vol) are displayed in Figure 3.

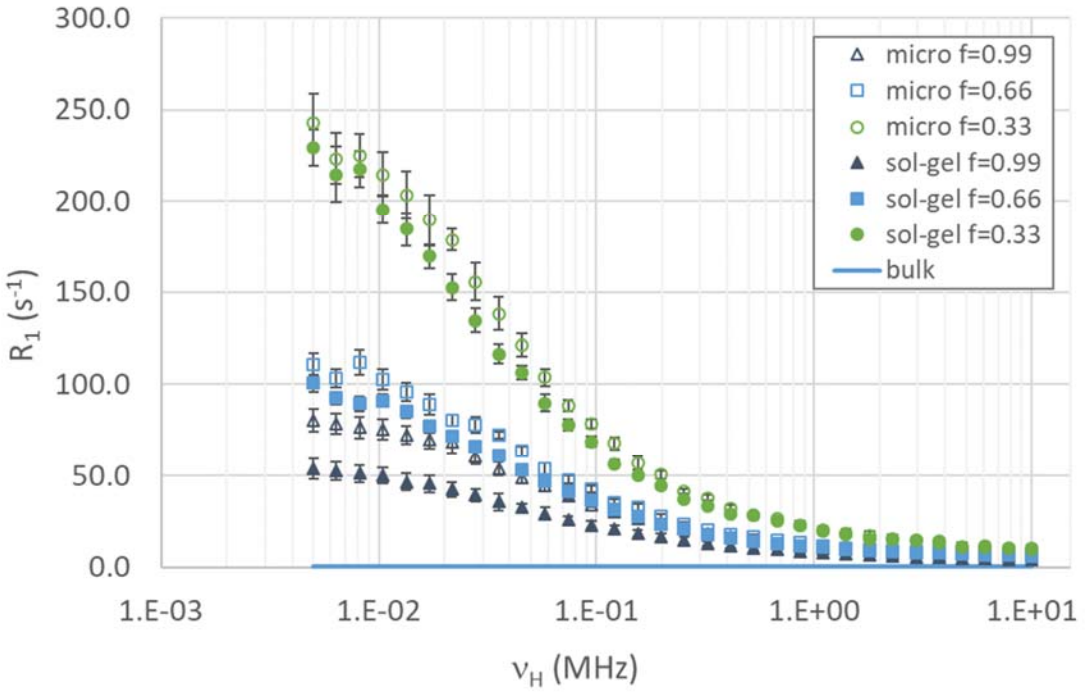

Figure 3. ^{1}H longitudinal relaxation rate (R_1 in s^{-1}) as a function of the frequency measurement (ν_H in MHz): microfluidic samples (open symbols), sol-gel samples: (filled symbols). Green circles: f = 0.33, blue squares: f = 0.66, dark blue triangles: f = 0.99. Continuous line corresponds to bulk water, for which no dispersion is obtained in this frequency range (R_{1b} = 0.41 s^{-1}).

Dispersions are clearly observed for both materials, the micro-fluidic and the standard one, indicating the effect of confinement on water. This dispersion can be related to the geometry

of the matrix (textural properties such as surface areas, porous volume and mesoporous arrangements) and/or to interactions between the matrix and confined water.

A measurement was first done using a sample hydrated with heavy water in order to evaluate intra- and intermolecular contributions to the water relaxation. The microfluidic bioglass was thus filled at $f = 0.99$ with heavy water D_2O, and longitudinal ^1H relaxation was measured for the residual protons in HOD and compared with the relaxation obtained with H_2O at the same filling degree (Figure 4)

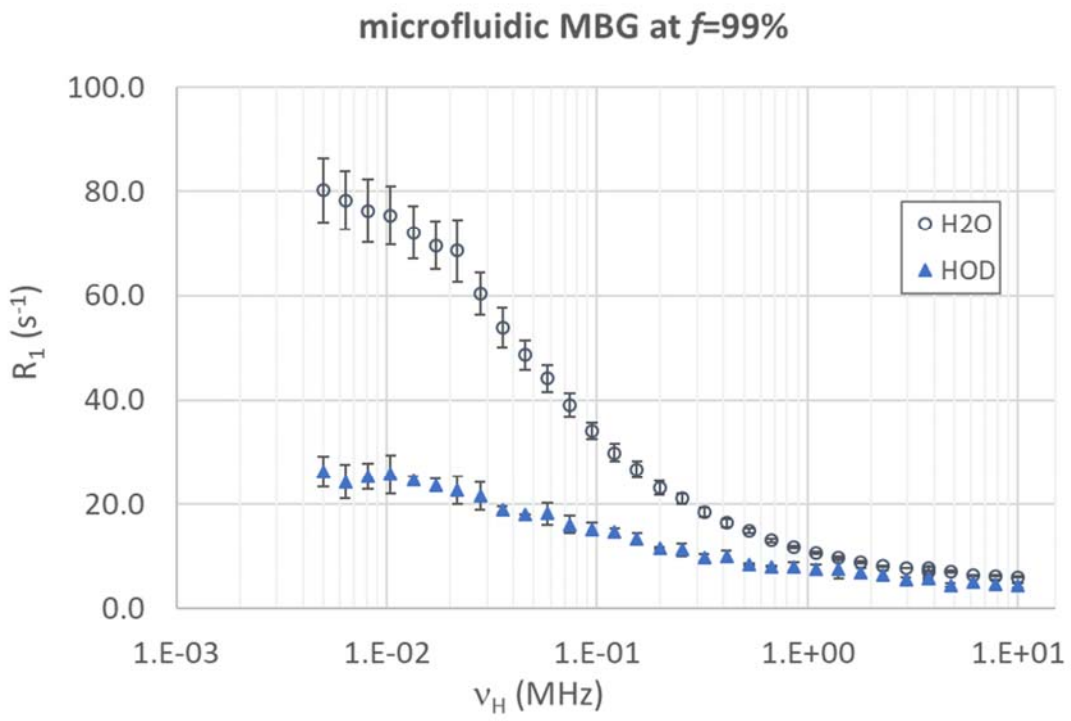

Figure 4. ^1H NMRD (R_1 in s^{-1} as a function of ν_H in MHz) in a microfluidic sample hydrated at 99 % vol. Dark blue open circles: hydration with H2O, Blue filled triangles: hydration with D_2O.

HOD relaxation being purely intermolecular, the comparison of H_2O and HOD dispersion curves shows that the ^1H low frequency relaxation of H_2O is mainly due to intramolecular dipolar interactions modulated by molecular reorientations[33]. For all R_1 measurements, i.e. in the whole Larmor frequency range studied (5 kHz – 10 MHz) and for every sample, magnetization recovery curves exhibit a mono-exponential behavior and ^1H R_1 values tend toward the one of water in bulk liquid (0.41 s^{-1}) as the filling degree increases (figure 3). This indicates that the exchange rate between free water molecules (denoted bulk) and the ones experiencing strong interactions with the surface (denoted adsorbed) is fast compared to the longitudinal relaxation rate. In this frame of "two-phase fast exchange model"[34] , it is an averaged longitudinal relaxation rate that is measured:

$$\boldsymbol{R_1(\omega_H) = p_a R_{1a}(\omega_H) + (1 - p_a) R_{1b}} \quad \textbf{(eq.1)}$$

with $R_{1a,b}$ the ^1H longitudinal relaxation rate of water in the free state (b) or in the adsorbed phase (a), p_a the water population in the adsorbed phase, and $\omega_H = 2\pi\nu_H$ the ^1H resonance frequency expressed in $rad.s^{-1}$

R_{1b}, the ^1H longitudinal relaxation rate of water in the free state, is constant with the ^1H resonance frequency (extreme narrowing condition) and the value of 0.41 s^{-1} was used considering that it is the same whatever the kind of bioglass, standard or microfluidic. The variation of the NMRD profiles with the filling factor *f* was analyzed according to eq.1 in order to compare the ^1H longitudinal relaxation rate of water in the adsorbed phase in the two samples. It is indeed known that, in partially filled pores, population in the adsorbed phase p_a varies with the filling factor *f* as[35] :

$$\boldsymbol{p_a = \frac{\lambda S}{V}\frac{1}{f}} \quad \textbf{(eq.2)}$$

With λ the width of the adsorbed water layer, S the porous surface area, and V the porous volume

Combining eq.1 and eq.2 leads to:

$$\boldsymbol{R_1(\omega_H) - R_{1b} = \frac{\lambda S}{V}(R_{1a}(\omega_H) - R_{1b})\ \frac{1}{f}} \qquad \textbf{(eq.3)}$$

The quantity $\frac{\lambda S}{V}(R_{1a}(\omega_H) - R_{1b})$ was thus retrieved with the linear evolution of $(R_1(\omega_H) - R_{1b})$ as a function of $\frac{1}{f}$. Results are displayed in Figure 5.

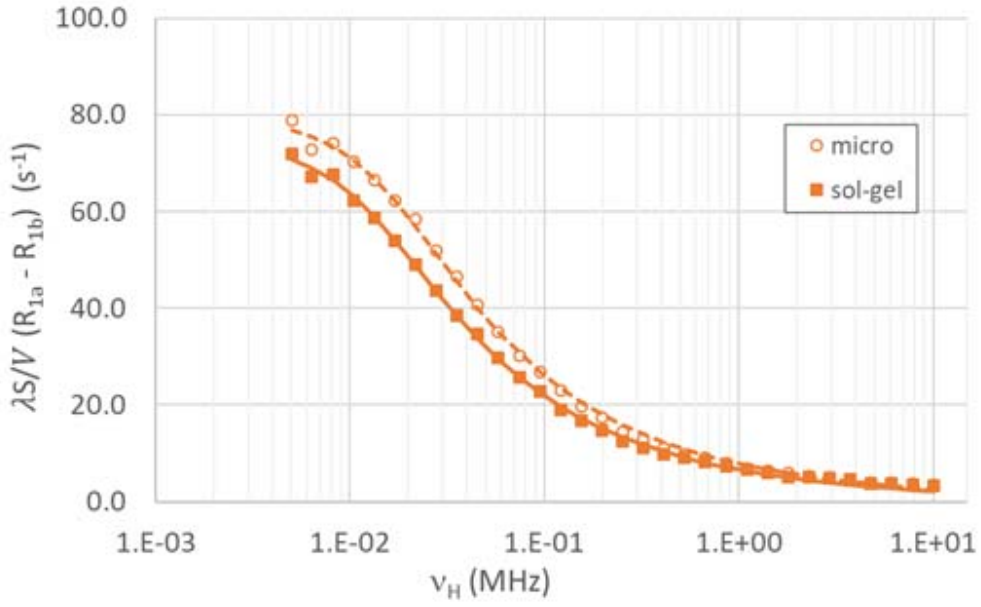

Figure 5. Comparison of the extracted longitudinal relaxation time of water in the adsorbed state in microfluidic bioglass (open symbols) and in standard sol-gel bioglass

(filled symbols). Lines (dashed for microfluidic bioglass and continuous for standard sol-gel bioglass) represent the best fits obtained with the model given in the text.

As previously shown, the observed dispersion in figure 5 is due to intramolecular dipolar interactions modulated by molecular reorientations of the water molecules at the pore surface. Relaxation rates were thus analyzed considering dipolar relaxation of like-spins ($R_{1a}(\omega_H) = K_d(J(\omega_H) + 4J(2\omega_H))$), and the motional model used for the spectral density $J(\omega)$ calculation considers an intermittence of adsorption steps at the interface and excursions into the bulk. From this model we can distinguish 2 characteristic times: τ_m characterizes the intermittent dynamics in the proximity of the pore surface [36,37] and τ_{esc} characterizes the escape of the molecules towards the bulk[38](NMRD asymptotic behavior). Results are summarized in Table 2.

Sample	τ_{esc} (μs)	τ_m (ps)	$\frac{\lambda S}{V}$
Sol-gel	**6.2**	**6.0**	**0.27**
Microfluidic	**5.1**	**6.0**	**0.32**

Table 2. Parameters obtained from the fit of the experimental data (shown in Fig. 5) with the model of intermittent motion of the adsorbed water molecules at the pores surface. τ_m characterizes the intermittent dynamics and τ_{esc} is the residence time before escaping to the bulk. The fitted effective dipolar coupling constant in both samples is $K_d = 2.5\ 10^9\ s^{-2}$.

The same value of τ_m (6.0 ps) is obtained in both MBGs, indicating that the water dynamics in the proximity of the pore surface is the same. The apparent shift between the NMRD profiles (fig.5) is actually mainly due to the different S/V ratios in the two MBGs. The width of the absorbed layer obtained from the ratios $\frac{\lambda S}{V}$ (Table 2) and $\frac{S}{V}$ (Table 1) is around 5 Å in both samples, consistent with a length obtained with 1-2 water molecule diameters. τ_m is related to both the average adsorption time at the surface (characterized by a time τ_a) and the minimal loop duration for excursion into the bulk (characterized by a time τ_l)[36]. Assuming τ_l in the order of the lifetime of one hydrogen bond in this kind of silica material (12 ps)[39] gives a value of 21 ps for τ_a using the relation $\tau_m = \frac{2\tau_a^2}{\pi\tau_l}$. Finally, we can show that τ_{esc} is slightly lower in the microfluidic sample compared to the standard one, indicating a faster escaping to the bulk for water confined in the microfluidic MBG. This may be due to the microcapsule organization of the microfluidic MBG, therefore structural information, obtained by ^{1}H Solid State NMR, should provide further understanding of how the grain architecture impacts the behavior of confined water. Since fast molecular motion obscures that structural information, low temperature experiments are mandatory; Differential Scanning Calorimetry is therefore recommended to determine the thermodynamic behavior of the confined water.

3.2. DSC curves:

For better understanding the phase changes and different structural reorganization that occur inside these porous bioglasses, we performed a differential scanning calorimetry

analysis. The cooling and heating DSC curves for water confined in both sol-gel and microfluidic MBGs at different volume hydration levels are shown in Figure 6 and typical results are obtained. Indeed, in the heating curves, we observe only one large peak with a maximum located at about 260 K for both microfluidic and sol-gel MBGs. This endothermic peak corresponds to the melting of the confined pore water. One notes that the position of this heating peak is not very sensitive to the degree of pore filling. Furthermore, the fact that the heating scan exhibits a single melting peak indicates that the mass transport process between all the different phases is quite fast. However, for the cooling scans, more subtle effects are observed and the cooling curves exhibit two or three peaks depending on the hydration level.

(a)

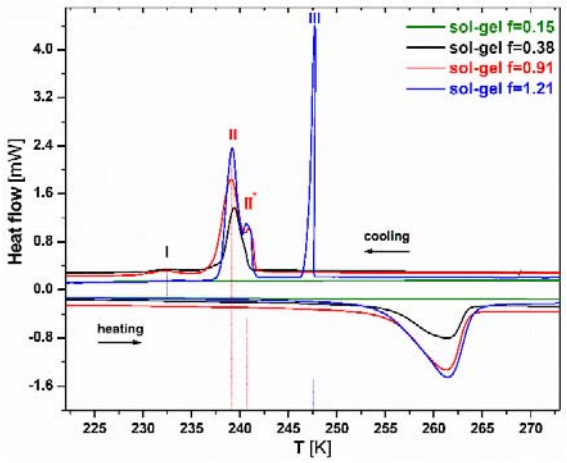

(b)

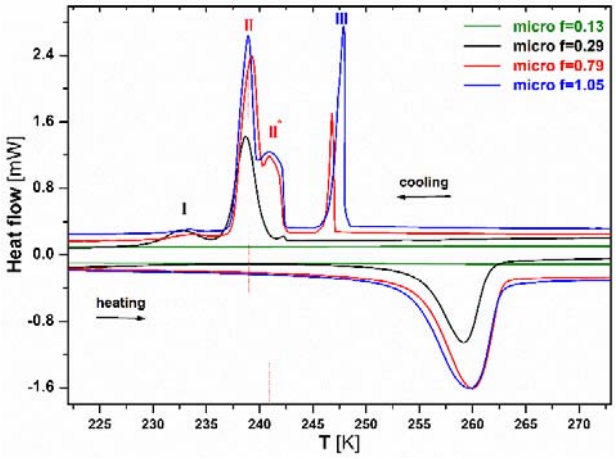

Figure 6. Results of differential scanning calorimetry: (a) hydrated standard sol-gel MBG at f = 0.15, 0.38, 0.91, 1.21 and (b) hydrated Microfluidic MBG at f = 0.13, 0.29, 0.79 and 1.05.

These results are in good agreement with the findings reported in the literature[6,25], indicating a non-homogenous freezing process for confined water due the coexistence of different phases and structural organization of confined water: distorted ice-like structure and bonded water films (one to three-molecules thick layers) next to the pore walls. It is however important to note, that for low relative pore fillings ($f < 0.2$), the DSC measurements are not sensitive enough to show any signature corresponding to a phase transition or to a structural organization.

For intermediate pore filling, the cooling curves for both MBGs showed two main exothermic peaks with maxima at 239 K and 233 K corresponding to site **II** and site **I** respectively. The peaks corresponding to site **II** are observed for all pore fillings ($f > 0.2$) and can be attributed to the liquid-solid transition of the confined pore water. The broad DSC peak with maxima at 233 K (site **I**) can be attributed to the subtle structural reorganization

of the bonded water film at the pore walls. One notes that, the DSC peak corresponding to site **I** is hardly visible in samples with high pore fillings (higher hydration level). This can be explained by the fact that for higher pore fillings, only a small fraction of the confined water is located in the boundary layer at the pore walls. Similar behavior has also been discussed by Schreiber and co-workers[6] and by Findenegg *et al*[40] in their works on water confined in a series of MCM-41 and SBA-15 silica. However, the attribution of these peaks has been the subject of interesting debate in the literature. The interpretation suggested by Findenegg *et al*[40] that the peak associated to site **I** is caused by delayering transitions of the liquid-like film has been questioned and instead, it was proposed that this transition is related to liquid-liquid transitions of interfacial water[41]. Other studies have demonstrated that some interfacial water layers, in interaction with the pore surface, are unfreezable, and thus associate the peak at 233 K (site **I**) to the reorganization of the boundary layer of unfreezable water adsorbed at the pore walls[6, 42] . This structural reorganization is also associated with a variation in the density of confined species. Indeed, in a recent neutron diffraction study, Zanotti et *al*[30] showed that the structural organization of this interfacial water is induced by the sudden change in the density of adsorbed water. This change is correlated with the modification of the hydrogen bond network as a result of interactions between interfacial water molecules and silica.

On increasing the hydration level, one observes an interesting behavior on the scans of the sol-gel sample hydrated at 91 % vol and that of the microfluidic sample hydrated at 79 % vol. The thermograms exhibit “hybrid peaks” and shoulder in the 240-246 K temperature range for both samples. However, a supplementary peak at around 246 K was observed in the microfluidic sample. This may be attributed to the liquid-solid transition of water in the

cavity of microspheres. It is noteworthy that the microfluidic sample exhibit a hollow inside the microcapsules (~100 μm) with a soft-like thin shell with a thickness of about 1 μm[10], while the sol-gel MBG have a dense appearance with a high degree of coalescence[8].

For the samples with excess water (105 % for the microfluidic MBG and 121 % for the sol-gel MBG) we observe an additional peak (site **III**) with a typical sharp onset at 248 K; this is assigned to the liquid-solid transition of super cooled water outside the MBG pores.

The calorimetric analysis clearly show that the phase transitions and the structural organization of the water confined in the pores of these MBGs is dependent on the filling ratio. For relative low pore fillings, the unfreezable interfacial pore layer is filled first and exhibits a structural reorganization associated to (site **I**). On increasing the amount of water, additional layers cover the interfacial adsorbed water. These new layers form the "intermediate" pore water (site **II**) and exhibit different thermodynamic properties corresponding to liquid-solid phase transition. For overloading with high water content, bulk-like water thermodynamic properties are observed (site **III**). The obtained results suggest that the thermodynamic behavior of confined water is quite similar in both MBGs with subtle differences that cannot be discussed in detail due to the sensitive limitation of the DSC technique. To obtain more insight on the properties of the different confined species, we applied MAS NMR spectroscopy as an appropriate approach that allows the structural analysis of the confined water.

3.3. ^{1}H MAS NMR spectra:

As mentioned earlier, analyzing water distribution and structuring inside the pores of MBGs can provide a detailed understanding of how the synthesis affects the water dynamics in the materials. Relying on the information provided by the DSC analysis, we therefore apply ^{1}H MAS NMR to study the MBGs at different hydration levels as a function of temperature.

In general, ^{1}H-MAS-NMR spectra of hydrated silicates exhibit several overlapped lines, which correspond to the different ^{1}H environments inside the mesopores [21–23]. These observed hydrogen signals originate from surface –SiOH groups and from water molecules inside the hydrophilic materials. Additionally, at room temperature it must be considered that dynamic exchange effects, like molecular reorientations of the water molecules, rotations of the surface –SiOH groups and proton transfer, will cause averaging of the chemical shifts[21]. Upon the addition of water, many possible hydrogen bonding configurations coexist between the water molecules and the various silanols present on the MBGs surface. For each configuration of a water molecule interacting with the surface and other water molecules, the ^{1}H are characterized by specific chemical shifts that are modulated by reorientation dynamics that are faster than the NMR timescale.

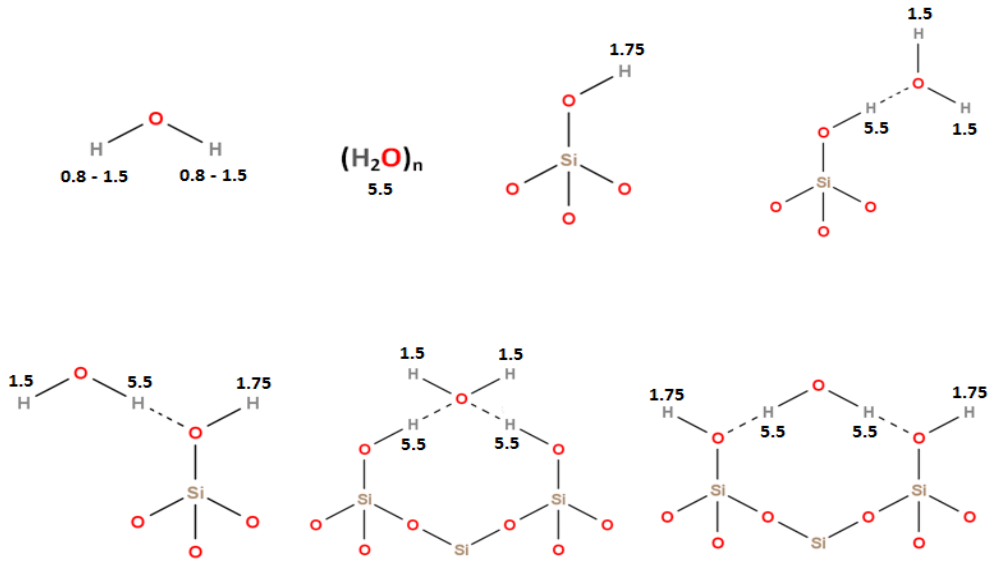

Figure 7. Possible –OH groups in the water/silica materials and the corresponding chemical shifts in ppm (TMS) [22,23]

Interestingly, the gradual adsorption of water in two mesoporous silica materials with cylindrical pores of uniform diameter, MCM-41(D_P = 3.3 nm) and SBA-15 (D_P = 8 nm) has also been studied previously at room temperature by ^{1}H MAS-NMR[23]. In that study, the spectra of dry materials with almost no water content exhibited a single resonance at 1.74 ppm, corresponding to surface SiOH protons. As soon as some water was added to the material, the surface SiOH signal was replaced by a new signal around 2.5 ppm. For the SBA-15 samples, increasing the water filling above a filling factor f = 0.08 resulted mainly in a single signal, shifting continuously from 3.9 ppm towards the bulk water chemical shift of 5 ppm as the pore filling was increased. Comparing these chemical shifts with the values given for the possible chemical shifts of –OH groups (Fig. 7) it is evident that none of these shifts

match the observed chemical shifts. This is explained by fast proton transfer and the dynamics of water molecules on the pore surface, that lead to the averaging of chemical shifts from the different configurations to a value between 3 and 5.5 ppm depending on the water content and the temperature. The evolution of ^{1}H chemical shifts as a function of water filling in SBA-15, has therefore been interpreted as a radial-pore-filling mode since filling occurs smoothly from the pore wall towards the center of the pore, inducing an average chemical shift that progressively tends towards the inner-bulk water value. Conversely inside MCM-41, when water content was increased, protons exhibited a bimodal line distribution of chemical shifts, with one peak at the position of inner-bulk water at 4.8 ppm, and the second peak in the range of water molecules adsorbed on surface SiOH groups at 3.4 ppm (for intermediate water filling with f = 0.23). This was therefore interpreted as an axial-pore-filling mode where, after the initial wetting, the water layer in pore grows axially in the direction of the pore axis. This difference in the filling modes was explained by the different pore diameters, 8 nm for the SBA-15 and 3.3 nm for the MCM-41, which lead to early coalescence of the surface water layers when filling narrow pores.

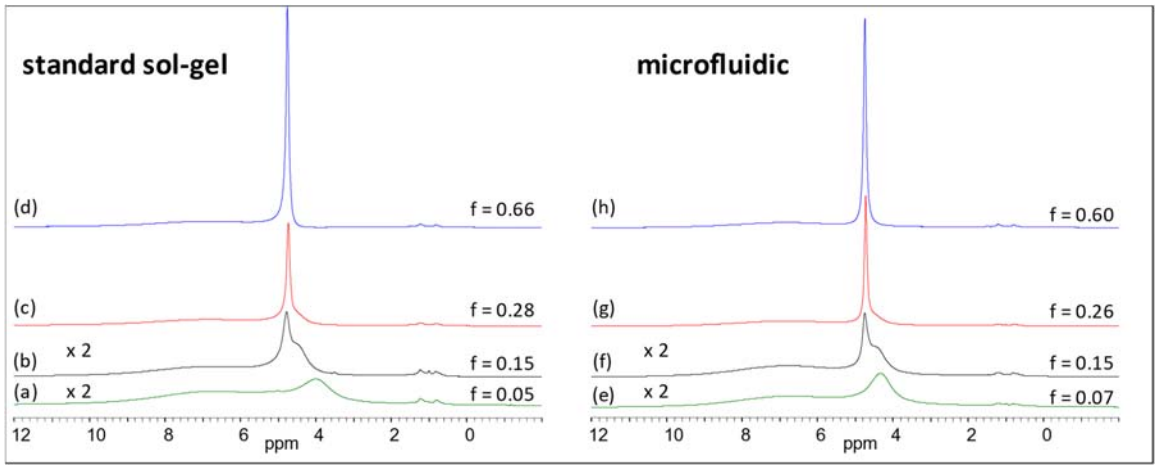

Figure 8. ^{1}H MAS spectra (ν^{MAS} = 12.5 kHz) of sol-gel (left) and microfluidic (right) MBGs for different HOD filling factors: f = 0.05 (a); 0.15 (b); 0.28 (c); 0.66 (d) and 0.07 (e); 0.15 (f); 0.26 (g); 0.60 (h) at 298 K. Intensities of spectra a, b, and e, f have been multiplied by 2 for sensitivity reasons.

Figure 8 displays ^{1}H MAS spectra of our hydrated MBGs for different HOD contents at 298 K. Regarding our materials, the MAS spectrum of the standard sol-gel MBG sample with the lowest water content (f = 0.05) exhibits mainly a peak around 4 ppm corresponding to interacting water and silanol protons. Additionally, the broad line between 6 and 8 ppm is assigned to interacting surface silanols[22] and strongly adsorbed water molecules, possibly blocked in surface heterogeneities. A similar spectrum is observed for the microfluidic MBG for a water filling factor f = 0.07. At intermediate water contents (f = 0.15) mainly two overlapped peaks are visible. As for the signal observed for lower water contents, the peak centered around 4.5 ppm corresponds to surface adsorbed water molecules and shifts continuously when hydration increases from f = 0.05 to 0.15. The second has a chemical shift of 4.8 ppm which corresponds to the value of bulk water clusters in the center of the pores[23]. Finally, for completely filled pores the adsorbed water signal has practically disappeared and only the free water signal is observed. The coexistence of two peaks at intermediate water content therefore points towards an axial filling mechanism for both MBGs. The fact that the ^{1}H chemical shift evolution as a function of the hydration is similar for the two MBGs is consistent with their similar pore diameters and pore surfaces.

At room temperature, water molecule dynamics prevent full separation of all the contributions from the different ^{1}H environments in both MBGs. In order to slow down these dynamics and suppress the chemical shift averaging, ^{1}H MAS NMR measurements were also performed at low temperature. Reducing the temperature affects the ^{1}H MAS NMR spectra of the sol-gel MBG (f = 0.4), as illustrated in figure 9 for temperatures down to 205K.

Down to 276 K, the spectrum of the sol-gel MBG exhibits mainly a single signal that broadens and shifts from 4.8 ppm to 5.5 ppm when temperature is reduced. This ^{1}H chemical shift range typically corresponds to free water clusters at this temperature. At the base of this signal, the broadly distributed signal (6-8 ppm) of strongly H-bound protons shows no significant evolution when temperature is reduced. Conversely, upon further decrease of the temperature, the 5.5 ppm peak continues to increase in width and can be decomposed into three main contributions resonating at 4.7 ppm, 5.6 ppm and 6.6 ppm.

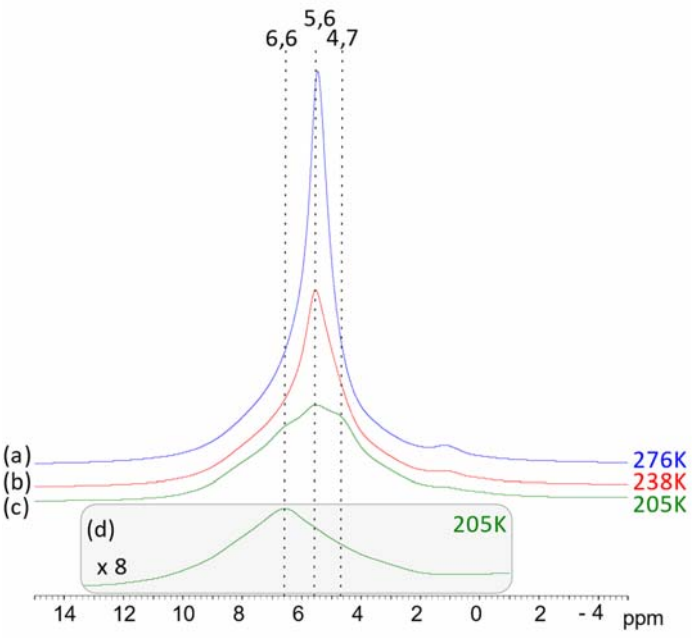

Figure 9. Temperature dependence of the centerbands of ^{1}H MAS NMR spectra (ν^{MAS} = 9 kHz) of standard sol-gel MBG hydrated with HOD at f = 0.4. Spectra are acquired at (a) 276 K, (b) 238 K, (c) 205 K. The insert (d) corresponds to the first spinning sideband of spectrum (c) aligned with the centerband; this signal is multiplied by a factor 8 for sensitivity reasons.

This behavior is consistent with the phase transitions observed by DSC. On figure 9 (d) the first spinning sideband of the spectrum acquired at 205 K is aligned with the spectral centerbands acquired at 276 K, 238 K and 205 K. This comparison illustrates the fact the only the peak at 6.6 ppm gives rise to significant chemical shift anisotropy ($\delta = \delta_{zz}-\delta_{iso} \approx -22$ ppm) and MAS sidebands. This signal can therefore be assigned to protons of solid water in the center of the pores that undergo a liquid/solid phase transition towards an amorphous or brittle ice phase[43] corresponding to the transition **site II** on the DSC thermograms (figure 6). Since the two others peaks don't show significant increase of MAS spinning sidebands, we therefore assign them to two types of mobile water protons. We interpret these as 3D super-cooled liquid water pools resonating around 5.6 ppm, and a slightly more shielded 2D single layer of surface adsorbed liquid water resonating around 4.7 ppm because of less hydrogen bonding. This rearrangement in a 2D surface water layer corresponds to the transition **site I** observed by DSC. According to our results from NMR relaxometry, and to numerous experimental studies[42,44] on the behavior of water in mesoporous hydrophilic matrices, we can indeed distinguish two types of water: free water in the middle of pores and adsorbed water adjacent to the pore wall. The liquid-solid phase transition of confined water has been studied intensively and it has been shown that on cooling, the intermediate free water

transforms into cubic ice and its stability increases with respect to the hexagonal phase on decreasing the temperature[43]. It is also well known that the layer of water in contact with the pore wall remains liquid[45,46] even at lower temperatures. This phase of super-cooled water remains confined between the surface of the pore wall and the solid phase of the free water in center of the pore. This phase is of particular interest because it was evidenced through numerous techniques that changes in its structural and dynamical behaviors occur at the temperature range observed here, between 240 K and 230 K. It was also suggested that water exhibits a liquid−liquid phase transition corresponding to the transition of a High Density Liquid (HDL) phase into a Low Density Liquid (LDL) phase upon decreasing the temperature[47]. In the light of these results, we interpret the temperature effects on the ^{1}H signal in the following way:

Similarly to what has been observed by Sattig et al[48], by decreasing the temperature, a liquid-solid transition of the inner water leads to the formation of solid water (signal at 6.6 ppm). Further lowering of the temperature induces a liquid/liquid reorganization at the pore surface that affects the hydrogen bond network of the supercooled water. As observed by Zanotti et al[47], the liquid/liquid reorganization induces a structural interfacial water heterogeneity with the coexistence of 2D LDL low density monolayer patches (signal 4.7 ppm) interacting mainly with the silica surface, and 3D HDL high density monolayer pools (signal at 5.6 ppm) of adsorbed water molecules additionally interacting with multiple other water molecules.

As a consequence of this structural behavior, in order to compare the structural distribution of the water confined in the two MBGs, ^{1}H MAS NMR measurements are best performed below the phase transition temperatures observed here. As seen on figure10, we

therefore compared the low temperature ^{1}H MAS signal evolution for both hydrated MBGs, as a function of the HOD filling factors.

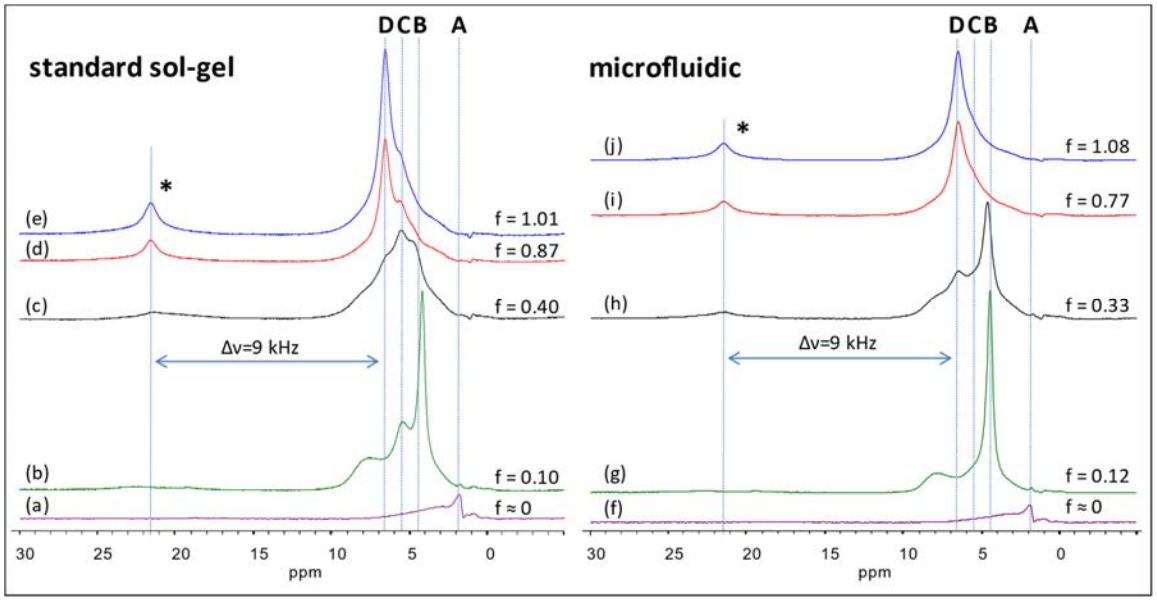

Figure 10. ^{1}H MAS spectra (ν^{MAS} = 9 kHz) of sol-gel (left) and microfluidic (right) MBGs for different HOD filling factors: f ≈ 0 (a); 0.10 (b); 0.40 (c); 0.87 (d)); 1.01 (e) and 0 (f); 0.12 (g); 0.33 (h); 0.77 (i); 1.08 (i) at 205 K. The first spinning sideband area is centered around 21ppm and marked by *.

The figure shows that the spectral evolution of both MBG materials is quite similar. The MAS spectra for the dried MBGs exhibits mainly a peak at 1.9 ppm (**site A**) and a broad component centered around 3.6 ppm, similar to what has been observed at room temperature for other dry mesoporous materials like MCM-41 and SBA-15[23]. These signal can be assigned to anhydrate hydroxyl groups and hydrogen bonded hydroxyl groups respectively[21]. As expected, anhydrate hydroxyl proton resonances seen in dry MBGs disappear as water is

introduced into the pores; they are replaced by new signals corresponding to protons of interacting water molecules and hydrated silanol groups. As water is introduced into the pores of MBGs (f = 0.10-0.12), the main signal shifts from 1.9 ppm to 4.7 ppm indicating the formation of the adsorbed 2D water layer (**site B**). The additional signal at 5.6 ppm (**site C**) is assigned to protons of 3D water pools discussed earlier, whereas the signal at 7.7 ppm can be assigned to protons of strongly bound surface water stuck in structural surface inhomogeneities, or defects as observed in SBA-15[23]. Upon further increase of the water content (f = 0.33-0.40) an additional signal at 6.6 ppm (**site D**) appears. As discussed earlier, this site exhibits MAS CSA sidebands and therefore corresponds to ice solid water. Above this filling factor, MBG spectra are dominated by this ice water peak.

Although all signals are present for both materials, it is clear that the 3D water pools (**signal C**) are more pronounced in the standard sol-gel MBG than in the microfluidic material. To better understand the heterogeneity of water populations inside the MBGs, we decomposed the spectra in its signal components using the Dmfit software[32] and plotted the relative surface area of peaks B, C and D as function of hydration at 205 K in Figure 11.

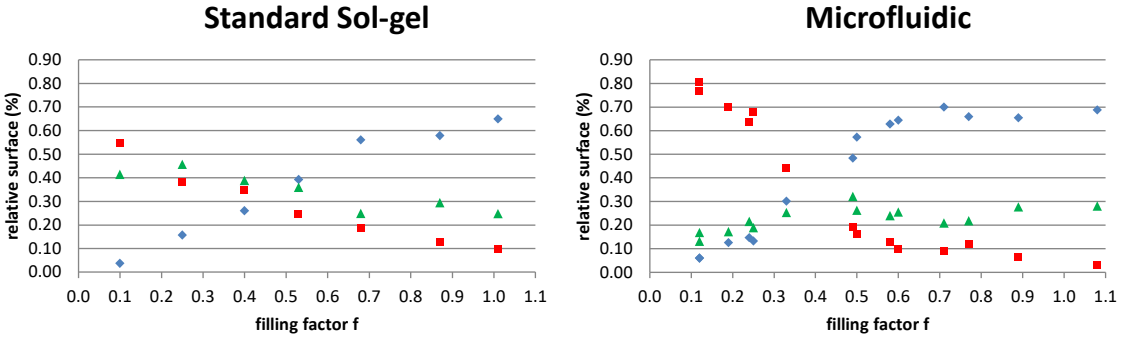

Figure 11: Relative area of ^{1}H signals B (squares, 2D water layer), C (triangles, 3D water pools) and D (diamonds, ice) at 205 K. The results for the sol-gel and microfluidic MBG are respectively presented on the left and right side.

These plots clearly show that for low water content the liquid phase in the microfluidic MBG contains predominantly 2D water, while in the sol-gel MBG the two types of liquid water (2D and 3D) already coexist. The fact that the 3D water pools are more present in the sol-gel MBG can be partly explained by the larger specific surface in the microfluidic MBG which is also in agreement with the relaxometry measurement, showing that $\frac{\lambda S}{V}$ is more important in the microfluidic MBG (table 2). Nevertheless, if all the specific surface was easily water accessible, the first layer of water molecules should only be filled at a pore filling factor f = 0.19 and 0.22 for the sol-gel and microfluidic MBG respectively. The significant presence of 3D water pools in the sol-gel MBG, already at a filling f = 0.1, therefore indicates that the full porous volume of the sol-gel MBG is less easily accessible to water than that of the microfluidic MBG.

To study further the water accessibility to the full porous volume, we plot in figure 12 the ratio of total liquid water (2D + 3D) with respect to ice as a function of hydration at 205 K.

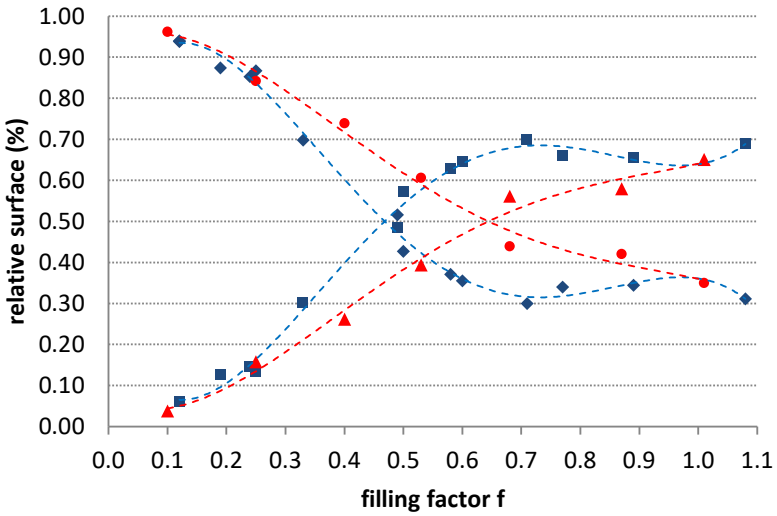

Figure 12. Relative area of rigid and mobile ^{1}H signals as a function of the filling factor f at 205 K. Data from the sol-gel MBG are presented in red dots (water, peak B+C) and triangles (ice, peak D). Data from the microfluidic MBG are presented in blue diamonds (water, peak B+C) and squares (ice, peak D). The polynomial interpolation lines are only drawn as guide to the eye to highlight the differences in the data evolution.

At water filling below f = 0.3, the water is mainly present in the liquid state for both MBGs. Above f = 0.3 the proportion of liquid water decreases in favor of solid water. It is interesting to note that the slopes are more pronounced for the microfluidic MBG, which indicates that for this material less hydration is needed to start filling the space at the pore center where water can organize to freeze into the solid state.

On the overall, the comparison of the ^{1}H MAS NMR spectra of the two MBGs indicate a significant heterogeneity of the water distribution in the sol-gel MBGs that is absent for the

microfluidic MBGs. This provides evidence that the full porous volume of the microfluidic MBG is more easily accessible to water than that of the sol-gel MBG. Since no evidence for differences in surface silanol densities was found from additional ^{29}Si NMR measurements, we speculate that the reason lies in the hollow microsphere structural feature of the microfluidic MBG, which facilitates the diffusion of water inside the pores. In particular, this interpretation is also consistent with the faster escaping to the bulk, observed by relaxometry, for water molecules adsorbed on the microfluidic MBG pore surface layer.

4. CONCLUSION:

In summary, the combination of thermal properties obtained by differential scanning calorimetry, with ^{1}H NMR properties obtained by field-cycling NMR relaxometry and MAS NMR spectroscopy, allowed the comparison of the respective dynamical and structural features of confined water inside two mesoporous bioglasses (MBGs). Although the MBGs have the same composition, one was synthesized by a standard sol gel procedure whereas the second was prepared through a microfluidic procedure.

The room temperature ^{1}H MAS NMR structural study of the two materials, as a function of hydration, indicated a similar axial pore filling mechanism and no significant difference between the two MBGs. Dynamical characterization, based on low-field NMR relaxometry, distinguished the presence of two water populations inside the materials: a ~5 Å thick water layer interacting with the pore surface, and a bulk type water confined in the center of the pores. These two populations were also distinguished by the DSC analysis where the rearrangement of the surface layer was detected about 10K lower than the typical liquid/solid phase transition of the water confined in the pore center. Performing the

hydration dependent ^{1}H MAS NMR study, at a temperature below the phase transitions observed by DSC, allowed again to distinguish the different water populations and indicated that at these temperatures the pore surface water remains liquid and rearranges into 2D monolayer patches and 3D water pools.

In these conditions, subtle quantitative differences could be observed between the two MBGs complementing the dynamical characterization from ^{1}H NMR relaxometry. In agreement with the smaller specific surface in the sol-gel MBG compared to the microfluidic material, relaxometry measurements showed that slightly less water is interacting with the pore surface in the sol gel MBG (according to $\frac{\lambda S}{V}$). This was expressed in the low temperature MAS study of the sol gel MBG, by a larger amount of 3D water with respect to 2D water. Nevertheless, the extent of the difference with the microfluidic material, especially for the lowest filling factors, also indicates that the full porous surface of the sol-gel MBG is less accessible to water than that of the microfluidic MBG. This interpretation was further reinforced by the analysis of the fraction of frozen water as a function of hydration and by the results from room temperature ^{1}H NMR relaxometry, showing that water molecules from the pore surface layer escape faster to the bulk inside the microfluidic MBG (according to τ_{esc}).

Since the MBGs studied here have the same composition, we explain these results by the microcapsule organization of the microfluidic MBG where the hollow microspheres facilitate the diffusion of water inside the pores of the material. In view of these results, we believe that the organization of microfluidic MBGs microcapsules will facilitate ion exchange with surrounding biological fluids, which will improve the adsorption behavior and

bioactivity of microfluidic MBG. To better understand the effect of the organization of microcapsules on the bioactive properties of MBGs, in vitro bioactivity tests will be carried out in a subsequent study.

ACKNOWLEDGEMENTS:

Authors would like to thank Dr. Nizar Bchellaoui and Dr. Abdel Illah El Abed (Laboratoire Lumière Matière et Interfaces (LuMIn), ENS-Paris Saclay, Centrale Supélec) for ensuring the microfluidic synthesis of the samples. The authors greatly acknowledge the Plateforme de RMN de l'Institut Jean Barriol, Université de Lorraine. This work was supported by the Université de Lorraine, the CNRS and the Institut Jean Barriol, which are gratefully acknowledged. H. Khoder is indebted to the French Ministry of Research for a doctoral fellowship.

REFERENCES:

(1) L. L. Hench, J. Wilson, Science 1984, 226, 630 –636.
(2) El-Fiqi, A.; Kim, T.-H.; Kim, M.; Eltohamy, M.; Won, J.-E.; Lee, E.-J.; Kim, H.-W. Capacity of Mesoporous Bioactive Glass Nanoparticles to Deliver Therapeutic Molecules. *Nanoscale* **2012**, *4* (23), 7475. https://doi.org/10.1039/c2nr31775c.
(3) Turdean-Ionescu, C.; Stevensson, B.; Izquierdo-Barba, I.; García, A.; Arcos, D.; Vallet-Regí, M.; Edén, M. Surface Reactions of Mesoporous Bioactive Glasses Monitored by Solid-State NMR: Concentration Effects in Simulated Body Fluid. *The Journal of Physical Chemistry C* **2016**, *120* (9), 4961–4974. https://doi.org/10.1021/acs.jpcc.5b12490.
(4) Izquierdo-Barba, I.; Arcos, D.; Sakamoto, Y.; Terasaki, O.; López-Noriega, A.; Vallet-Regí, M. High-Performance Mesoporous Bioceramics Mimicking Bone Mineralization. *Chemistry of Materials* **2008**, *20* (9), 3191–3198. https://doi.org/10.1021/cm800172x.
(5) Izquierdo-Barba, I.; Salinas, A. J.; Vallet-Regí, M. In Vitro Calcium Phosphate Layer Formation on Sol-Gel Glasses of the CaO-SiO2 System. *Journal of Biomedical Materials Research* **1999**, *47* (2), 243–250. https://doi.org/10.1002/(SICI)1097-4636(199911)47:2<243::AID-JBM15>3.0.CO;2-S.
(6) Schreiber, A.; Ketelsen, I.; Findenegg, G. H. Melting and Freezing of Water in Ordered Mesoporous Silica Materials. *Physical Chemistry Chemical Physics* **2001**, *3* (7), 1185–1195. https://doi.org/10.1039/b010086m.
(7) Morishige, K.; Kawano, K. Freezing and Melting of Water in a Single Cylindrical Pore: The Pore-Size Dependence of Freezing and Melting Behavior. *The Journal of Chemical Physics* **1999**, *110* (10), 4867–4872. https://doi.org/10.1063/1.478372.

(8) Buntkowsky, G.; Vogel, M.; Winter, R. Properties of Hydrogen-Bonded Liquids at Interfaces. *Zeitschrift für Physikalische Chemie* **2018**, *232* (7–8), 937–972. https://doi.org/10.1515/zpch-2018-1110.
(9) Letaïef, N.; Lucas-Girot, A.; Oudadesse, H.; Dorbez-Sridi, R.; Boullay, P. Investigation of the Surfactant Type Effect on Characteristics and Bioactivity of New Mesoporous Bioactive Glass in the Ternary System SiO2–CaO–P2O5: Structural, Textural and Reactivity Studies. *Microporous and Mesoporous Materials* **2014**, *195*, 102–111. https://doi.org/10.1016/j.micromeso.2014.03.035.
(10) Andersson, N.; Kronberg, B.; Corkery, R.; Alberius, P. Combined Emulsion and Solvent Evaporation (ESE) Synthesis Route to Well-Ordered Mesoporous Materials. *Langmuir* **2007**, *23* (3), 1459–1464. https://doi.org/10.1021/la0622267.
(11) Bchellaoui, N.; Hayat, Z.; Mami, M.; Dorbez-Sridi, R.; El Abed, A. I. Microfluidic-Assisted Formation of Highly Monodisperse and Mesoporous Silica Soft Microcapsules. *Scientific Reports* **2017**, *7* (1). https://doi.org/10.1038/s41598-017-16554-4.
(12) Crupi, V.; Longo, F.; Majolino, D.; Venuti, V. Raman Spectroscopy: Probing Dynamics of Water Molecules Confined in Nanoporous Silica Glasses. *The European Physical Journal Special Topics* **2007**, *141* (1), 61–64. https://doi.org/10.1140/epjst/e2007-00018-x.
(13) Chathoth, S. M.; Mamontov, E.; Kolesnikov, A. I.; Gogotsi, Y.; Wesolowski, D. J. Quasielastic Neutron Scattering Study of Water Confined in Carbon Nanopores. *EPL (Europhysics Letters)* **2011**, *95* (5), 56001. https://doi.org/10.1209/0295-5075/95/56001.
(14) Andreani, C.; Colognesi, D.; Mayers, J.; Reiter, G. F.; Senesi, R. Measurement of Momentum Distribution of Lightatoms and Molecules in Condensed Matter Systems Using Inelastic Neutron Scattering. *Advances in Physics* **2005**, *54* (5), 377–469. https://doi.org/10.1080/00018730500403136.
(15) Buntkowsky, G.; Vogel, M. Small Molecules, Non-Covalent Interactions, and Confinement. *Molecules* **2020**, *25* (14), 3311. https://doi.org/10.3390/molecules25143311.
(16) Stapf, S.; Kimmich, R.; Seitter, R.-O.; Maklakov, A. I.; Skirda, V. D. Proton and Deuteron Field-Cycling NMR Relaxometry of Liquids Confined in Porous Glasses. *Colloids and Surfaces A: Physicochemical and Engineering Aspects* **1996**, *115*, 107–114. https://doi.org/10.1016/0927-7757(96)03610-2.
(17) Kimmich R. "Field-Cycling NMR Relaxometry: Instrumentation, Model Theories and Applications."
(18) Kimmich, R.; Anoardo, E. Field-Cycling NMR Relaxometry. *Progress in Nuclear Magnetic Resonance Spectroscopy* **2004**, *44* (3–4), 257–320. https://doi.org/10.1016/j.pnmrs.2004.03.002.
(19) Modig, K.; Pfrommer, B. G.; Halle, B. Temperature-Dependent Hydrogen-Bond Geometry in Liquid Water. *Physical Review Letters* **2003**, *90* (7). https://doi.org/10.1103/PhysRevLett.90.075502.
(20) Andrew, E. R.; Bradbury, A.; Eades, R. G. Nuclear Magnetic Resonance Spectra from a Crystal Rotated at High Speed. *Nature* **1958**, *182* (4650), 1659–1659. https://doi.org/10.1038/1821659a0.

(21) Walia, J.; Crone, J.; Liang, J.; Niknam, M.; Lemaire, C.; Terry Thompson, R.; Peemoeller, H. Temperature and Hydration Dependence of Proton MAS NMR Spectra in MCM-41: Model Based on Motion Induced Chemical Shift Averaging. *Solid State Nuclear Magnetic Resonance* **2013**, *49–50*, 26–32. https://doi.org/10.1016/j.ssnmr.2012.11.003.
(22) Trébosc, J.; Wiench, J. W.; Huh, S.; Lin, V. S.-Y.; Pruski, M. Solid-State NMR Study of MCM-41-Type Mesoporous Silica Nanoparticles. *Journal of the American Chemical Society* **2005**, *127* (9), 3057–3068. https://doi.org/10.1021/ja043567e.
(23) Grünberg, B.; Emmler, T.; Gedat, E.; Shenderovich, I.; Findenegg, G. H.; Limbach, H.-H.; Buntkowsky, G. Hydrogen Bonding of Water Confined in Mesoporous Silica MCM-41 and SBA-15 Studied by ^{1}H Solid-State NMR. *Chemistry - A European Journal* **2004**, *10* (22), 5689–5696. https://doi.org/10.1002/chem.200400351.
(24) Fouzri, A.; Dorbez-Sridi, R.; Oumezzine, M. Differential Scanning Calorimetry and X-Ray Diffraction Study of Water Confined in Silica Gel for Several Levels of Hydration. *The European Physical Journal Applied Physics* **2003**, *22* (1), 21–28. https://doi.org/10.1051/epjap:2003011.
(25) Kittaka, S.; Ishimaru, S.; Kuranishi, M.; Matsuda, T.; Yamaguchi, T. Enthalpy and Interfacial Free Energy Changes of Water Capillary Condensed in Mesoporous Silica, MCM-41 and SBA-15. *Physical Chemistry Chemical Physics* **2006**, *8* (27), 3223. https://doi.org/10.1039/b518365k.
(26) Weigler, M.; Brodrecht, M.; Buntkowsky, G.; Vogel, M. Reorientation of Deeply Cooled Water in Mesoporous Silica: NMR Studies of the Pore-Size Dependence. *J. Phys. Chem. B* **2019**, *123* (9), 2123–2134. https://doi.org/10.1021/acs.jpcb.8b12204.
(27) Lederle, C.; Sattig, M.; Vogel, M. Effects of Partial Crystallization on the Dynamics of Water in Mesoporous Silica. *J. Phys. Chem. C* **2018**, *122* (27), 15427–15434. https://doi.org/10.1021/acs.jpcc.8b03815.
(28) Yao, Y.; Fella, V.; Huang, W.; Zhang, K. A. I.; Landfester, K.; Butt, H.-J.; Vogel, M.; Floudas, G. Crystallization and Dynamics of Water Confined in Model Mesoporous Silica Particles: Two Ice Nuclei and Two Fractions of Water. *Langmuir* **2019**, *35* (17), 5890–5901. https://doi.org/10.1021/acs.langmuir.9b00496.
(29) Kittaka, S.; Sou, K.; Yamaguchi, T.; Tozaki, K. Thermodynamic and FTIR Studies of Supercooled Water Confined to Exterior and Interior of Mesoporous MCM-41. *Physical Chemistry Chemical Physics* **2009**, *11* (38), 8538. https://doi.org/10.1039/b905258e.
(30) Zanotti, J.-M.; Bellissent-Funel, M.-C.; Chen, S.-H. Experimental Evidence of a Liquid-Liquid Transition in Interfacial Water. *Europhysics Letters (EPL)* **2005**, *71* (1), 91–97. https://doi.org/10.1209/epl/i2004-10529-2.
(31) Thurber, K. R.; Tycko, R. Measurement of Sample Temperatures under Magic-Angle Spinning from the Chemical Shift and Spin-Lattice Relaxation Rate of 79Br in KBr Powder. *Journal of Magnetic Resonance* **2009**, *196* (1), 84–87. https://doi.org/10.1016/j.jmr.2008.09.019.
(32) Massiot, D.; Fayon, F.; Capron, M.; King, I.; Le Calvé, S.; Alonso, B.; Durand, J.-O.; Bujoli, B.; Gan, Z.; Hoatson, G. Modelling One- and Two-Dimensional Solid-State NMR Spectra. *Magnetic Resonance in Chemistry* **2002**, *40* (1), 70–76. https://doi.org/10.1002/mrc.984.

(33) Steiner, E.; Bouguet-Bonnet, S.; Blin, J.-L.; Canet, D. Water Behavior in Mesoporous Materials As Studied by NMR Relaxometry. *The Journal of Physical Chemistry A* **2011**, *115* (35), 9941–9946. https://doi.org/10.1021/jp205456g.
(34) Kimmich, R. Strange Kinetics, Porous Media, and NMR. *Chemical Physics* **2002**, *284* (1–2), 253–285. https://doi.org/10.1016/S0301-0104(02)00552-9.
(35) Mattea, C.; Kimmich, R.; Ardelean, I.; Wonorahardjo, S.; Farrher, G. Molecular Exchange Dynamics in Partially Filled Microscale and Nanoscale Pores of Silica Glasses Studied by Field-Cycling Nuclear Magnetic Resonance Relaxometry. *The Journal of Chemical Physics* **2004**, *121* (21), 10648–10656. https://doi.org/10.1063/1.1808423.
(36) Levitz, P.; Korb, J. P.; Petit, D. Slow Dynamics of Embedded Fluid in Mesoscopic Confining Systems as Probed by NMR Relaxometry. *The European Physical Journal E* **2003**, *12* (1), 29–33. https://doi.org/10.1140/epje/i2003-10046-2.
(37) Chemmi, H.; Petit, D.; Levitz, P.; Denoyel, R.; Galarneau, A.; Korb, J.-P. Noninvasive Experimental Evidence of the Linear Pore Size Dependence of Water Diffusion in Nanoconfinement. *The Journal of Physical Chemistry Letters* **2016**, *7* (3), 393–398. https://doi.org/10.1021/acs.jpclett.5b02718.
(38) CHEMMI. Chemmi H. (2011) "Diffusion Multi-Échelle et et Sorption Hydrique Dans Les Matériaux Cimentaires, PhD Thesis École Polytechnique.
(39) Renou, R.; Szymczyk, A.; Ghoufi, A. Water Confinement in Nanoporous Silica Materials. *The Journal of Chemical Physics* **2014**, *140* (4), 044704. https://doi.org/10.1063/1.4862648.
(40) Findenegg, G. H.; Jähnert, S.; Akcakayiran, D.; Schreiber, A. Freezing and Melting of Water Confined in Silica Nanopores. *ChemPhysChem* **2008**, *9* (18), 2651–2659. https://doi.org/10.1002/cphc.200800616.
(41) Brovchenko, I.; Oleinikova, A. 4 - Phase Diagram of Confined Water. In *Interfacial and Confined Water*; Brovchenko, I., Oleinikova, A., Eds.; Elsevier: Amsterdam, 2008; pp 91–119. https://doi.org/10.1016/B978-044452718-9.50005-8.
(42) Walther Hansen, E.; Schmidt, R.; Stöcker, M.; Akporiaye, D. Self-Diffusion Coefficient of Water Confined in Mesoporous MCM-41 Materials Determined by 1H Nuclear Magnetic Resonance Spin-Echo Measurements. *Microporous Materials* **1995**, *5* (3), 143–150. https://doi.org/10.1016/0927-6513(95)00053-C.
(43) Jelassi, J.; Castricum, H. L.; Bellissent-Funel, M.-C.; Dore, J.; Webber, J. B. W.; Sridi-Dorbez, R. Studies of Water and Ice in Hydrophilic and Hydrophobic Mesoporous Silicas: Pore Characterisation and Phase Transformations. *Phys. Chem. Chem. Phys.* **2010**, *12* (12), 2838. https://doi.org/10.1039/b908400b.
(44) Hansen, E. W.; Gran, H. C.; Sellevold, E. J. Heat of Fusion and Surface Tension of Solids Confined in Porous Materials Derived from a Combined Use of NMR and Calorimetry. *The Journal of Physical Chemistry B* **1997**, *101* (35), 7027–7032. https://doi.org/10.1021/jp9710594.
(45) Ishizaki, T.; Maruyama, M.; Furukawa, Y.; Dash, J. G. Premelting of Ice in Porous Silica Glass. *Journal of Crystal Growth* **1996**, *163* (4), 455–460. https://doi.org/10.1016/0022-0248(95)00990-6.

(46) Ishikiriyama, K.; Todoki, M. Evaluation of Water in Silica Pores Using Differential Scanning Calorimetry. *Thermochimica Acta* **1995**, *256* (2), 213–226. https://doi.org/10.1016/0040-6031(94)02174-M.
(47) Zanotti, J.-M.; Judeinstein, P.; Dalla-Bernardina, S.; Creff, G.; Brubach, J.-B.; Roy, P.; Bonetti, M.; Ollivier, J.; Sakellariou, D.; Bellissent-Funel, M.-C. Competing Coexisting Phases in 2D Water. *Scientific Reports* **2016**, *6* (1). https://doi.org/10.1038/srep25938.
(48) Sattig, M.; Vogel, M. Dynamic Crossovers and Stepwise Solidification of Confined Water: A 2H NMR Study. *J. Phys. Chem. Lett.* **2014**, *5* (1), 174–178. https://doi.org/10.1021/jz402539r.

TABLES :

Sample	$S_{BET}(m^2/g)$	V_P (cm^3/g)	D_P(nm)
Microfluidic MBG	514	0.76	5.9
Standard sol-gel MBG	376	0.66	5.7

Table 1. Textural parameters of MBGs: Specific surface area (S_{BET}), mesopore volume (V_P) and pore size (D_P), synthesized by combining sol gel and Microfluidic Method (Microfluidic MBG) and by standard sol-gel method (Standard MBG)

Sample	τ_{esc} (μs)	τ_m (ps)	$\frac{\lambda S}{V}$
Sol-gel	6.2	6.0	0.27
Microfluidic	5.1	6.0	0.32

Table 2. Parameters obtained from the fit of the experimental data (shown in Fig. 5) with the model of intermittent motion of the adsorbed water molecules at the pores surface. τ_m characterizes the intermittent dynamics and τ_{esc} is the residence time before escaping to the bulk. The fitted effective dipolar coupling constant in both samples is $K_d = 2.5\ 10^9\ s^{-2}$.

FIGURE CAPTIONS:

Figure1. a) SEM micrograph of the microfluidic MBG b) White field confocal microscopy images of the microfluidic MBG sample doped with fluorescein

Figure2. SEM micrograph of the standard sol-gel MBG surface

Figure 3. ^{1}H longitudinal relaxation rate (R1 in s^{-1}) as a function of the frequency measurement (ν_H in MHz): microfluidic samples (open symbols), sol-gel samples: (filled symbols). Green circles: f=0.33, blue squares: f=0.66, dark blue triangles: f=0.99. Continuous line corresponds to bulk water, for which no dispersion is obtained in this frequency range (R_{1b}=0.41 s^{-1}).

Figure 4. ^{1}H NMRD (R1 in s-1 as a function of ν_H in MHz) in a microfluidic sample hydrated at 99%vol. Dark blue open circles: hydration with H2O, Blue filled triangles: hydration with D_2O.

Figure 5. Comparison of the extracted longitudinal relaxation time of water in the adsorbed state in microfluidic bioglass (open symbols) and in standard sol-gel bioglass (filled symbols). Lines (dashed for microfluidic bioglass and continuous for standard sol-gel bioglass) represent the best fits obtained with the model given in the text.

Figure 6. Results of differential scanning calorimetry: (a) hydrated standard sol-gel MBG at f = 0.15, 0.38, 0.91, 1.21 and (b) hydrated Microfluidic MBG at f = 0.13, 0.29, 0.79 and 1.05.

Figure 7. Possible –OH groups in the water/silica materials and the corresponding chemical shifts in ppm (TMS)[20,21]

Figure 8. ^{1}H MAS spectra (ν^{MAS} = 12.5 kHz) of sol-gel (left) and microfluidic (right) MBGs for different HOD filling factors: f = 0.05 (a); 0.15 (b); 0.28 (c); 0.66 (d) and 0.07 (e); 0.15 (f); 0.26 (g); 0.60 (h) at 298 K. Intensities of spectra a, b, and e, f have been multiplied by 2 for sensitivity reasons.

Figure 9. Temperature dependence of the centerbands of ^{1}H MAS NMR spectra (ν^{MAS} = 9 kHz) of standard sol-gel MBG hydrated with HOD at f = 0.4. Spectra are acquired at (a) 276K, (b) 238K, (c) 205K. The insert (d) corresponds to the first spinning sideband of spectrum (c) aligned with the centerband; this signal is multiplied by a factor 8 for sensitivity reasons.

Figure 10. ^{1}H MAS spectra (ν^{MAS} = 9 kHz) of sol-gel (left) and microfluidic (right) MBGs for different HOD filling factors: f ≈ 0 (a); 0.10 (b); 0.40 (c); 0.87 (d)); 1.01 (e) and 0 (f); 0.12 (g); 0.33 (h); 0.77 (i); 1.08 (i) at 205 K. The first spinning sideband area is centered around 21ppm and marked by *.

Figure 11: Relative area of ^{1}H signals B (squares, 2D water layer), C (triangles, 3D water pools) and D (diamonds, ice) at 205K. The results for the sol-gel and microfluidic MBG are respectively presented on the left and right side.

Figure 12. Relative area of rigid and mobile ^{1}H signals as a function of the filling factor f at 205K. Data from the sol-gel MBG are presented in red dots (water, peak B+C) and triangles (ice, peak D). Data from the microfluidic MBG are presented in blue diamonds

(water, peak B+C) and squares (ice, peak D). The polynomial interpolation lines are only drawn as guide to the eye to highlight the differences in the data evolution.

FIGURES:

Figure1.

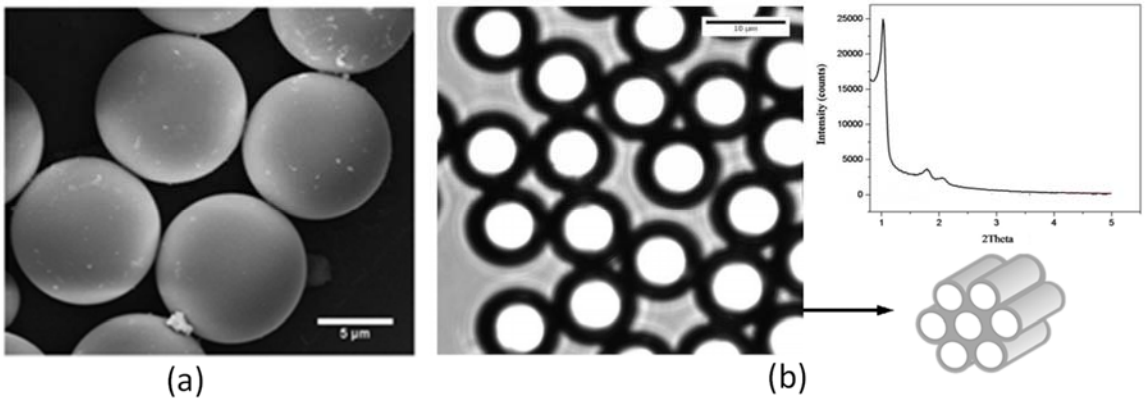

Figure2.

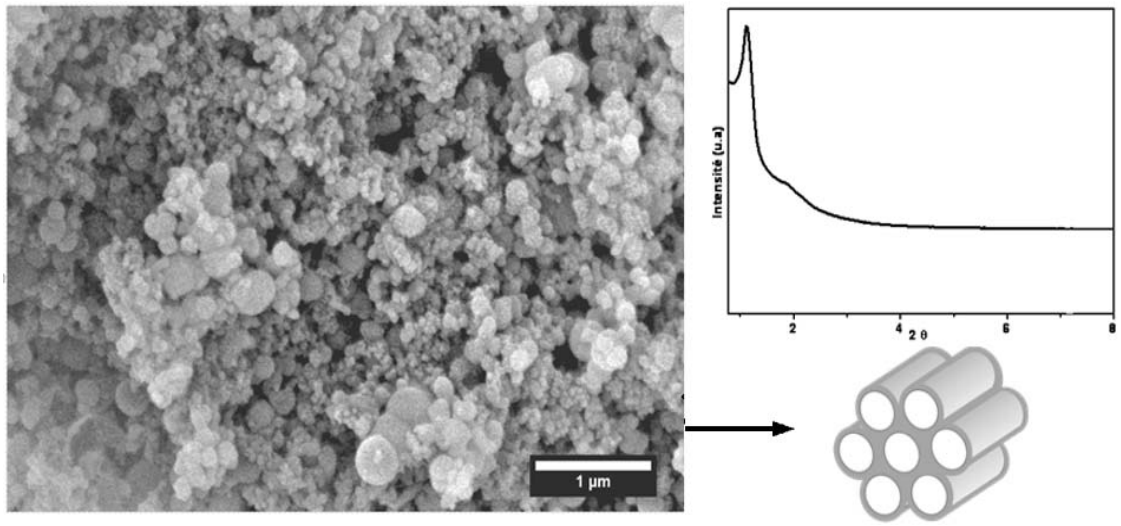

Figure3.

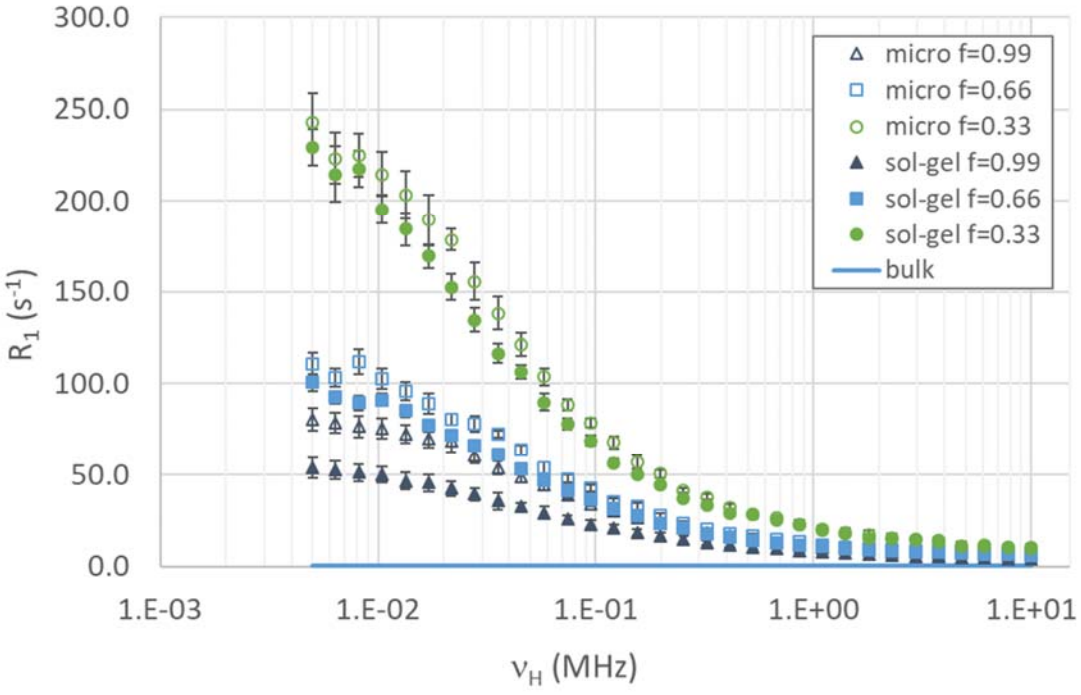

Figure4.

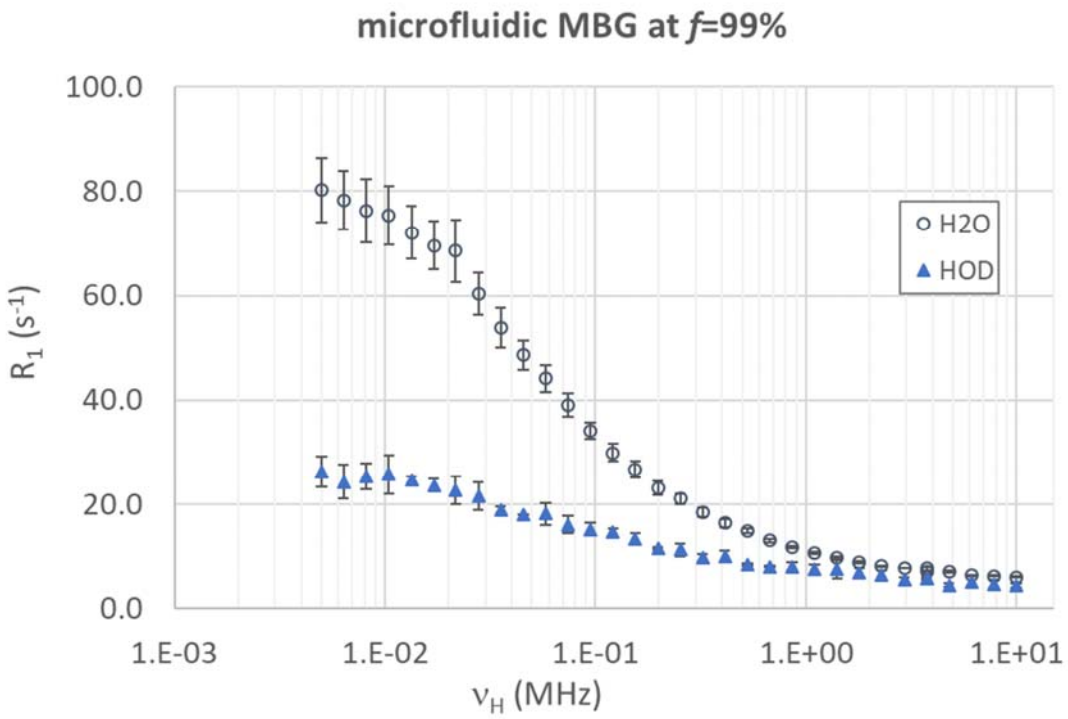

Figure5.

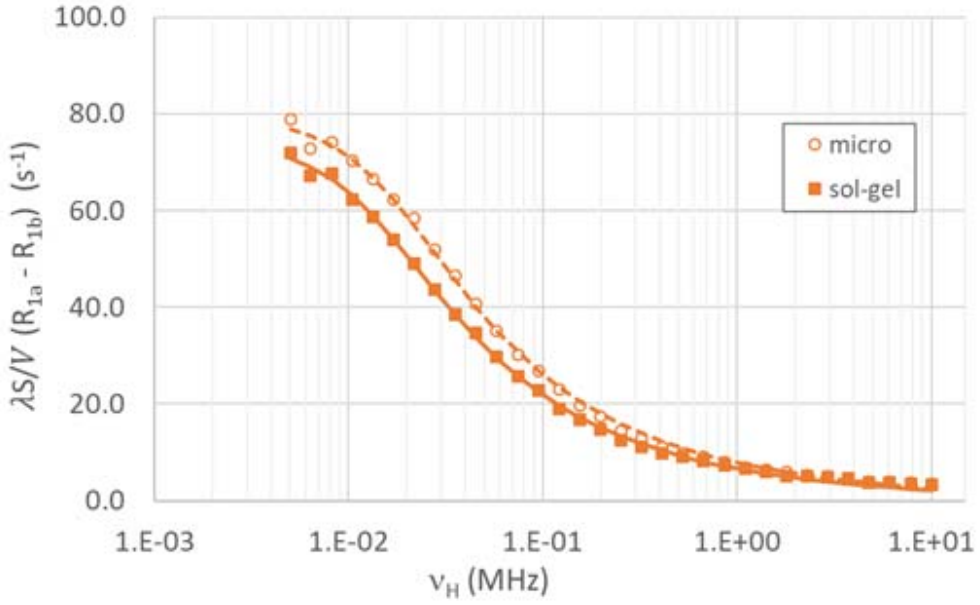

Figure6.

(a)

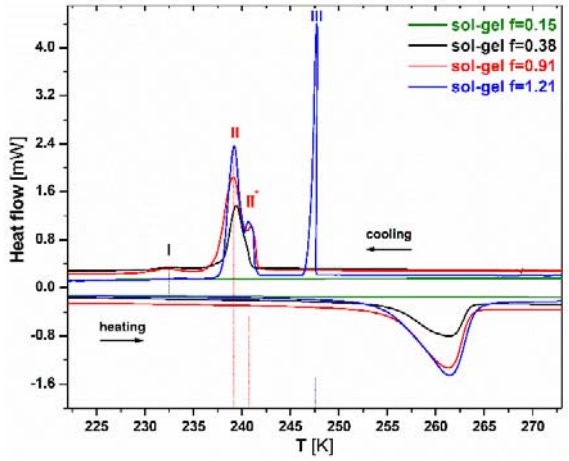

(b)

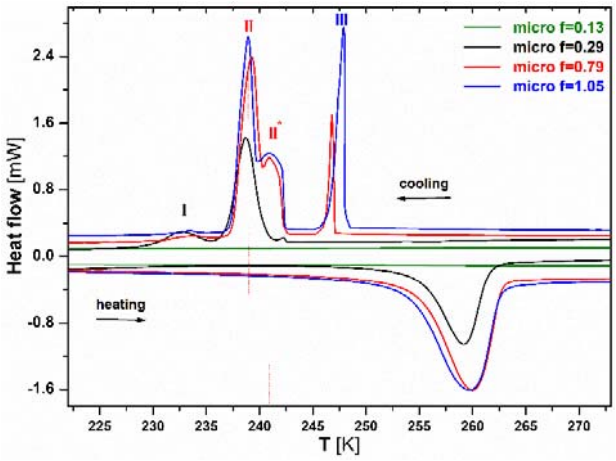

Figure7.

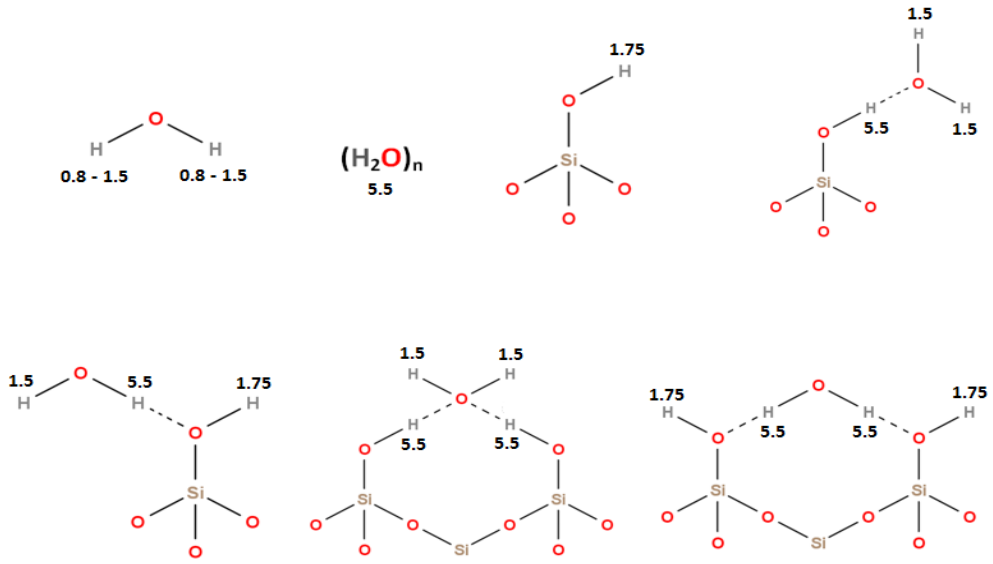

Figure 8.

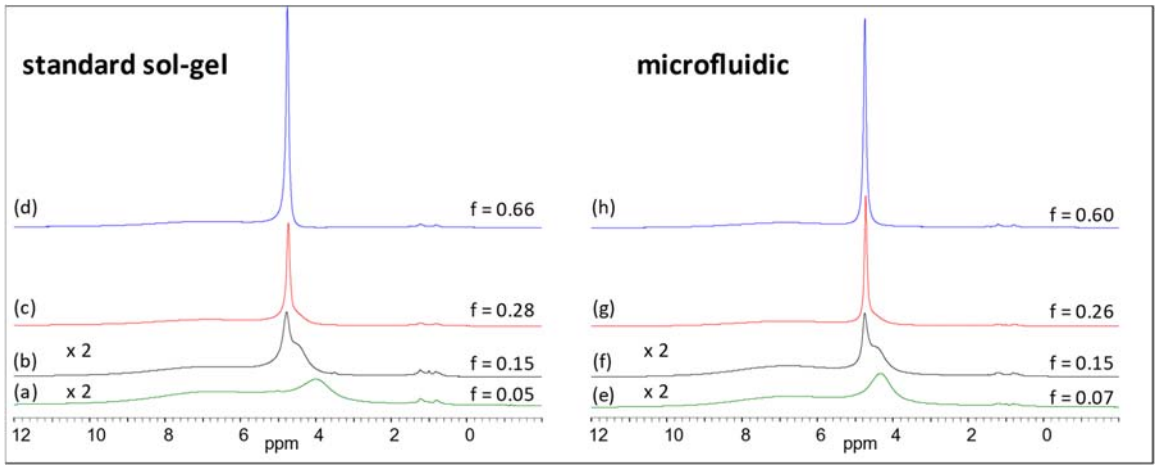

Figure 9.

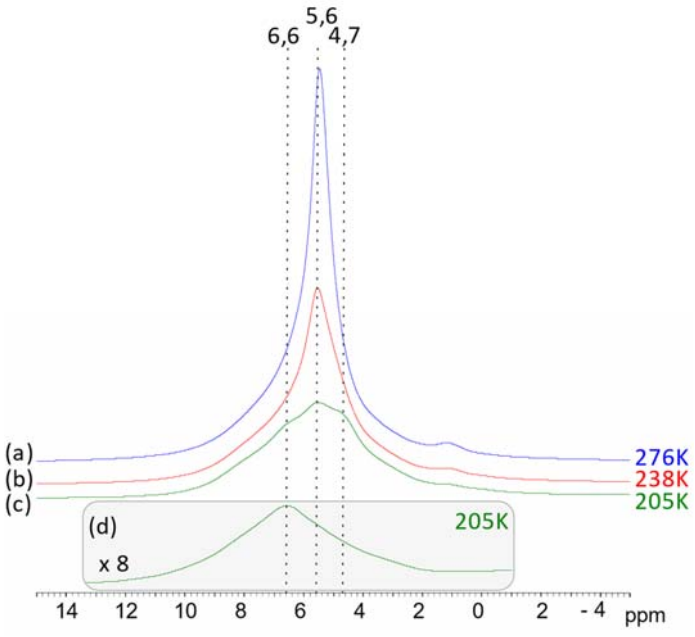

Figure 10.

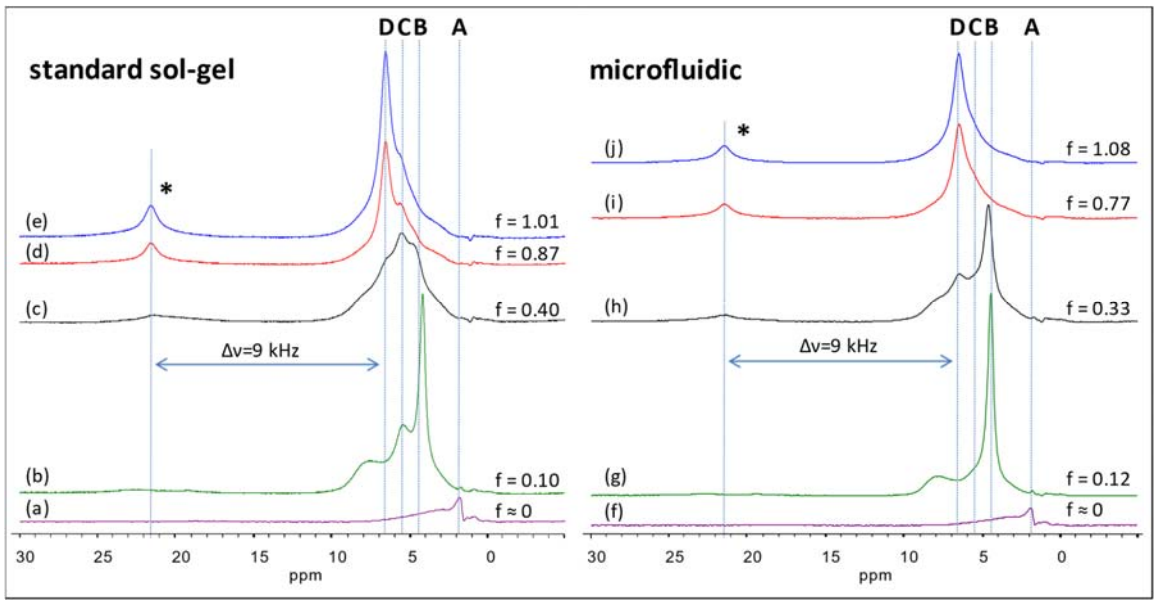

Figure 11.

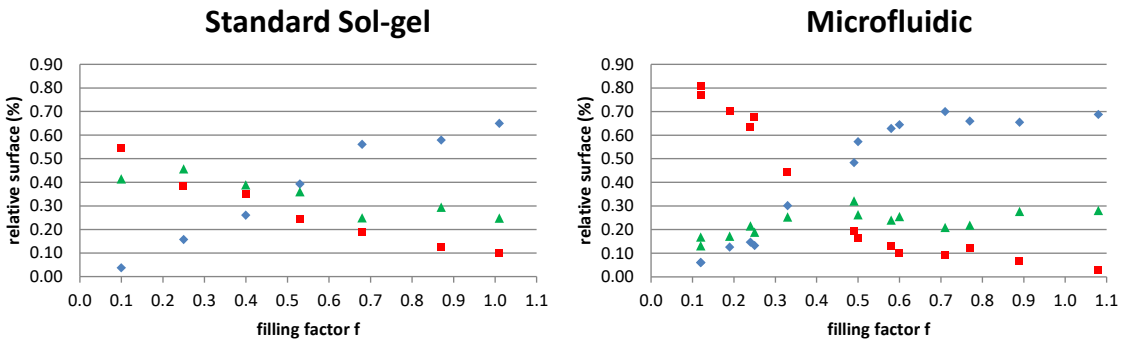
Standard Sol-gel
Microfluidic
relative surface (%)
filling factor f
0.00
0.10
0.20
0.30
0.40
0.50
0.60
0.70
0.80
0.90
0.0
0.1
0.2
0.3
0.4
0.5
0.6
0.7
0.8
0.9
1.0
1.1

Figure 12.

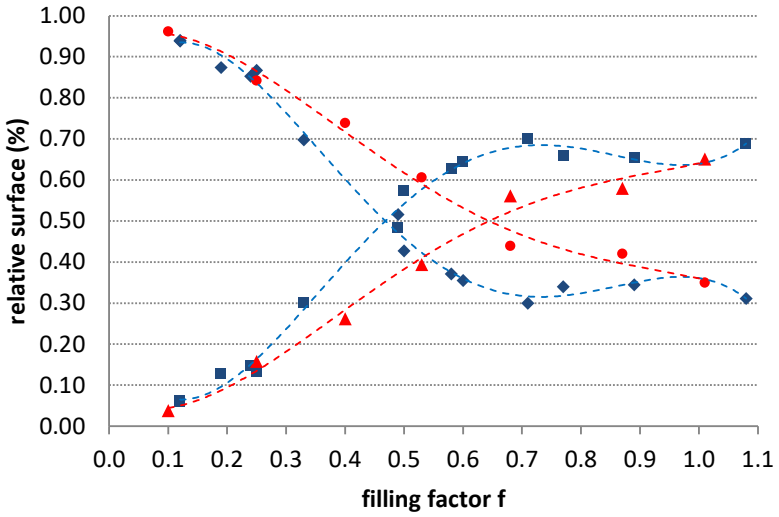
relative surface (%)
filling factor f
0.00
0.10
0.20
0.30
0.40
0.50
0.60
0.70
0.80
0.90
1.00
0.0
0.1
0.2
0.3
0.4
0.5
0.6
0.7
0.8
0.9
1.0
1.1